

Predicting calcification risk in prosthetic aortic valves: a hybrid physics-based and machine learning approach

Pascal Corso¹, Giorgia Tagliavini², Maria Giuseppina Chiara Nestola³, Fergal Brian Coulter⁴

Affiliations: ¹ETH Zurich, Swiss Data Science Center, Zurich, Switzerland. ²Swiss Federal Laboratories for Materials Science and Technology (Empa), Laboratory for Computational Engineering, Dübendorf, Switzerland. ³Università della Svizzera italiana (USI), Euler Institute, Lugano, Switzerland. ⁴ETH Zurich, Complex Materials group, Zurich, Switzerland.

Correspondence: Pascal Corso, ETH Zurich, Switzerland.

E-mail: `pascal.corso@sdsc.ethz.ch`

Abstract

Calcific degeneration remains the primary failure mode of bioprosthetic aortic valves and a growing concern for emerging polymeric alternatives. In this study, six prosthetic valve configurations combining two leaflet geometries (V-shaped scallop D1^V and U-shaped scallop D2^U) with three constitutive material models (synthetic elastomer, bovine pericardium and porcine tissue) are simulated throughout systole within a patient-specific curved aorta reconstructed from clinical CT data using a high-fidelity fluid-structure interaction framework. An incremental formulation of Finite-Time Lyapunov Exponents (FTLE) applied to the leaflet deformation gradients is introduced as a novel descriptor of structural point coherence on the leaflet surface. Together with wall shear stress (WSS) derived features, the FTLE field

is fed into an unsupervised k -means clustering algorithm that partitions each leaflet into
 four calcification risk classes without any fitting to experimental data. Validation against
 an experimentally calibrated calcification intensity map from micro-CT of explanted bovine
 pericardial valves yields a Spearman rank correlation of $\rho_S = 0.98$ and a Cohen’s weighted
 kappa of $\kappa_w = 0.91$ when the FTLE- and WSS-based classifications are combined, with an
 approximately equal optimal weighting ($w \approx 0.50$). The analysis reveals that porcine tissue
 concentrates strain into localised high-gradient zones whereas the isotropic elastomer dis-
 tributes strain uniformly yet generates elevated shear fluctuations through sustained leaflet
 flutter. The D2^U leaflet geometry paired with bovine pericardium emerges as the least
 susceptible configuration across both risk dimensions. By coupling leaflet structural point
 coherence with haemodynamic shear in a model-free framework, the proposed methodology
 provides a transferable design tool for ranking and evaluating next-generation prosthetic
 valve candidates with respect to calcification susceptibility.

Keywords Bioprosthetic and elastomeric heart valves; Calcification risk stratification;
 Computational fluid-structure interaction; Digital twin; Finite-time Lyapunov exponent;
 Unsupervised clustering.

1 Introduction

Calcific aortic valve stenosis is the most prevalent valvular heart disease, affecting up to 12% of the population above the age of 75^{39,48}. The condition involves progressive fibrosis and calcium phosphate deposition on the valve leaflets, restricting their motion, obstructing left ventricular outflow during systole and ultimately precipitating heart failure^{6,41}. Aortic valve replacement (AVR) has become the standard treatment for moderate to severe stenosis, with roughly 300,000 procedures performed worldwide each year, a number projected to double by 2050 owing to population ageing³⁸. The diseased valve is substituted either by a mechanical prosthesis, which necessitates lifelong anticoagulation therapy, or by a bioprosthetic aortic valve (BioAV) fashioned from biological tissue such as bovine pericardium or porcine tissue⁴¹. Bioprosthetic valves circumvent the drawbacks of mechanical prostheses yet suffer from structural valve degeneration; recurrent calcification remains the most frequent failure mode, limiting prosthesis lifespan and compelling reintervention^{48,49,45}. A synthetic-elastomer aortic valve (referred to throughout as ‘polymeric’ following prevailing convention, though collagen and elastin in bioprosthetic leaflets are chemically no less polymeric) represents a promising alternative combining the advantages of both mechanical and bioprosthetic replacement options, with the added benefit of personalising the prosthesis design to the patient’s aortic geometry and ventricular flow conditions^{14,44,17}.

Structural valve deterioration (SVD) is a complex, multiscale and multifactorial process in which mechanical fatigue and calcification of the biological tissue play central and intertwined roles¹⁷. In bioprosthetic valves made from glutaraldehyde-pretreated tissue, the fixation process devitalises residual cells, leaving phosphorus-rich cellular debris as primary nucleation sites for calcium phosphate precipitation; disruption of the calcium pump and depletion of native mineralisation inhibitors in these devitalised cells permit crystal growth at these sites, further compounded by the reactivity of residual aldehyde groups with circulating calcium ions^{46,17}. Both transplant-related factors (residual donor cells and debris, loss of glycosaminoglycans and collagen-elastin fibre damage during fixation and storage) and recipient-related factors (immune cell infiltration, serum proteolytic enzymes and calcium-

binding proteins) contribute to dystrophic calcification²⁵. As cyclic loading stretches the collagen network, fibril sliding and reorientation lead to progressive weakening and eventual failure of the load-bearing protein architecture^{49,17}; this fatigue-induced fibre damage has been identified as a complementary nucleation mechanism, particularly in the high-strain belly region of the leaflet^{48,49}. The interaction between fatigue and calcification is bidirectional: mineral deposits stiffen the tissue locally, amplify mechanical heterogeneity and redistribute cyclic stresses, promoting further damage in adjacent tissue and establishing a self-reinforcing mechanobiological feedback loop¹⁷. Increased surface roughness from mechanical degradation additionally enhances local turbulence and wall shear stress on the tissue, accelerating both fibre damage and mineral deposition^{17,5}. As reviewed comprehensively by Greco *et al.*¹⁷, curtailing SVD requires multiscale characterisation of the pericardium, from the nanostructure of individual collagen molecules to the macroscopic fatigue and haemodynamic performance of the valve, so that accurate structure-function relationships can inform computational models and next-generation prosthesis design. Synthetic-elastomer aortic valves are likewise susceptible to calcific degeneration, yet through a distinct pathway dominated by physicochemical ageing^{44,15,17}. Upon implantation, the polymeric surface triggers a foreign body inflammatory response in which recruited neutrophils and macrophages generate reactive oxygen species (ROS) that drive oxidative degradation of the polymer chains, fragmenting them and rendering the surface progressively more hydrophilic and polar⁴⁴. The resulting protein adsorption amplifies immune activation, whilst the release of calcium and phosphate ions from oxidatively damaged cell membranes promotes calcium phosphate precipitation on the altered surface⁴⁴. Local flow disruption and the ensuing increase in leaflet stiffness sustain a positive feedback loop, accelerating further mineral accumulation⁴⁴. Importantly, several steps in this cascade are directly governed by near-leaflet blood motion and local leaflet deformation, thereby motivating the computational investigation of both quantities in the present study.

From a haemodynamic standpoint, the wall shear stress (WSS) vector exerted by blood onto the leaflet surfaces, together with derived topological indicators including the oscillatory

shear index (OSI) and the topological shear variation index (TSVI), has been correlated with calcific damage on the leaflet surface and with deterioration of the arterial wall^{48,32,1}. Recent advances in fully coupled fluid-structure interaction (FSI) frameworks have demonstrated that leaflet flutter amplifies oscillatory shear and residence time, linking local flow-structure interactions to mechanisms that promote mineral accumulation^{17,11}. Tsolaki, Corso *et al.*⁴⁸ showed through a multiscale multimodal investigation that the spatial distribution of calcification in failed bovine pericardial valve explants could be predicted via a regression equation involving the TSVI and the time-averaged wall shear stress (TAWSS) from FSI simulations. Although the predictive capability of this approach was particularly promising (coefficient of determination $R^2 \approx 0.75$), it requires fitting of coefficients to experimental micro-CT data, limiting its applicability to new valve designs and material configurations for which no *ex vivo* calcification evidence exists.

From a dynamical systems standpoint, whether trajectories of neighbouring Lagrangian material points on the leaflet diverge or converge over time constitutes a complementary descriptor of the mechanical environment endured by the tissue. Finite-Time Lyapunov Exponents (FTLE), originally introduced to identify Lagrangian Coherent Structures (LCS) in fluid flows^{47,40}, can be repurposed to characterise the stretching and folding of the leaflet material. Computed from successive structural deformation gradients at the mesh nodes of the leaflet, the FTLE quantifies the maximal rate of divergence between neighbouring material points over a finite time horizon. Regions of elevated FTLE correspond to zones of pronounced material point separation rate, where intense and heterogeneous tissue deformations may promote collagen damage and ensuing mineral deposition. Although FTLE has been exploited in blood flow analyses to delineate jet boundaries and recirculation zones downstream of aortic valves^{47,40,11}, an incremental FTLE formulation applied directly to the leaflet strain field has not, to the best of our knowledge, been used as a predictor of calcification risk.

Machine learning has gained considerable traction in cardiovascular research, both for clinical risk stratification and for the post-processing of computational haemodynamic data.

Supervised approaches, including random forests and convolutional neural networks, have been applied to echocardiographic and CT imaging data to assist in diagnosing aortic valve disease and predicting post-operative outcomes^{21,20,27}. In the context of computational fluid dynamics, unsupervised clustering has emerged as an effective means of mapping haemodynamic risk without requiring labelled training data: k-means and related algorithms have been used to delineate regions of disturbed shear on arterial walls, classify oscillatory flow patterns in stenosed geometries and identify zones susceptible to atherosclerotic lesion formation^{16,34,33,7}. More recently, data-driven approaches have been extended to valve leaflet haemodynamics, extracting spatial features from WSS fields to relate near-wall flow characteristics to sites of endothelial dysfunction or calcification^{9,50}. Despite this growing body of work, joint unsupervised classification of leaflet calcification risk from both leaflet material point separation and haemodynamic shear descriptors remains unexplored.

In a prior two-part computational study^{11,12}, we investigated the interplay between valve architecture, jet flow configuration, vortex dynamics, spectral characteristics and kinetic energy anisotropy for two bioprosthetic valve designs implanted in a straight ascending aorta. That study revealed that leaflet geometry exerts a marked influence on downstream haemodynamics, and that the design referred to as Ulth0, characterised by a U-shaped scallop curve with a small belly length and nearly stable leaflets throughout systole, promotes a more organised and physiological flow compared to the V-shaped design VLth30, which exhibits non-axisymmetric flutter. Building upon these findings, the present work extends the computational framework in several directions. FSI simulations are carried out in a patient-specific curved aorta geometry reconstructed from clinical imaging data, introducing more physiological flow conditions. Two additional leaflet materials, namely porcine tissue and a silicone-based elastomer, are incorporated alongside the previously studied bovine pericardial material, yielding six valve configurations. An unsupervised machine learning methodology based on k-means clustering is then proposed to stratify the spatial distribution of calcification risk on the leaflet surfaces from the newly introduced incremental leaflet-strain-based FTLE along with WSS fields, without any need for fitting regression coefficients to experi-

mental data.

The objectives of the present study are threefold: (i) to simulate the coupled blood flow and valve dynamics during systole for six valve configurations arising from the combination of two leaflet geometries and three constitutive material models in a patient-specific aorta; (ii) to extract temporal features from the FTLE and WSS fields on the leaflets and to classify the calcification risk spatially through k-means clustering; (iii) to validate the unsupervised classification against experimentally calibrated calcification data⁴⁸ and to rank the six valve designs according to a comprehensive risk score. By combining leaflet material point coherence and haemodynamic shear information within a model-free clustering framework, we aim to furnish a predictive tool for comparing and refining prosthetic valve designs with respect to their susceptibility to calcific degeneration.

2 Materials and Methods

2.1 Valve leaflet geometry parametrisation and constitutive models for the leaflets

2.1.1 Mathematical description of leaflet geometries

Leaflet geometries can be thoroughly characterised from a parametric description relying on two curves: a belly curve and a scallop curve. The parametrisation is illustrated in Fig. 1A. Each valve comprises three identical leaflets attached to a common crown (or ring) of inner diameter \mathcal{D} , itself sutured to a patient-specific aorta model (Figs 1A and 2A). In the current study, the aorta geometry was reconstructed from computed tomography data of a randomised patient (male, 85 years) provided by the University Hospital Zurich and segmented using Materialise Mimics (Materialise NV, Leuven, Belgium). It incorporates the key anatomical features that shape the physiological flow field downstream of the prosthetic aortic valve^{11,17}: a curved patient-specific aortic lumen, extracted by lofting cross-sectional rings along an interpolated centreline, and an aortic root grafted from a separate scan, both

joined and filleted into a single smooth surface. The volumetric representation of the curved aorta was obtained by extruding the reconstructed surface to a wall thickness of 500 μm . A hollow cylindrical extension was appended upstream of the aortic annulus to represent the left ventricular outflow tract (LVOT) as illustrated in Fig. 2A. It is worth noting that the crown geometry is asymmetric, with each commissure featuring a slightly different thickness to accommodate the anatomical variation in the shapes of the three sinuses of Valsalva. Regarding the leaflets, five parameters in total govern their shape: three for the belly curve and two for the scallop curve (Fig. 1A). For the geometrical description of the two curves, we consider the centre of the coordinate system positioned at the intersection of the belly and attachment curves. The x-, y- and z- directions are the radial, circumferential and axial directions, respectively.

The belly curve (red curve in Fig. 1A and B) controls the cross-sectional profile of the leaflet in the radial-axial plane. The belly height coordinate, Z_{belly} , along the axial direction (normalised coordinate \mathbf{x}) is given by a hyperbolic sine function:

$$Z_{\text{belly}}(\mathbf{x}) = a_{\text{sinh}} \cdot \sinh\left(\frac{\mathbf{x}}{b_{\text{sinh}}}\right) \cdot h_{\text{belly}} \cdot \frac{\mathcal{D}}{2}, \quad (1)$$

where a_{sinh} and b_{sinh} are shape parameters and h_{belly} is the factor multiplying the aortic root radius, $\frac{\mathcal{D}}{2}$, to control the belly height. The scallop curve (blue curve in Fig. 1A and B) dictates the attachment line connecting each leaflet to the ring. Its height coordinate, Z_{scallop} , along the circumferential direction (normalised coordinate \mathbf{y}) is described by a power law (Fig. 1A):

$$Z_{\text{scallop}}(\mathbf{y}) = \mathbf{y}^{n_{\text{power}}} \cdot \frac{\mathcal{D}}{2} \cdot (\tan(\theta_{\text{scallop}}) + h_{\text{belly}}), \quad (2)$$

with n_{power} the exponent and θ_{scallop} the inclination angle between the belly extremity and the commissure. The three-dimensional leaflet surface is obtained by sweeping and blending these two curves along the circumferential direction (Fig. 1A).

[Figure 1 about here.]

[Figure 2 about here.]

2.1.2 Leaflet geometrical parameter values

In the present study, a unified nomenclature for the leaflet designs is adopted to replace the less intuitive naming conventions used in previous works^{11,48}. Each design is labelled as $Dn^{\mathcal{S}}$, where n is a sequential integer identifier and $\mathcal{S} \in \{U, V\}$ indicates the shape of the scallop (attachment) curve according to the corresponding letter. The two leaflet geometries introduced in the present work are then referred to as $D1^V$ and $D2^U$ (see Figs 2A and 1B). In addition, the three leaflet designs from earlier studies are re-labelled as follows for consistency: $ULth0^{48,4} \rightarrow D3^U$, $VLth30^{11,48} \rightarrow D4^V$ and $Ulth0^{11} \rightarrow D5^U$. The corresponding geometrical parameters, obtained by fitting each leaflet shape to the mathematical description presented above, are summarised in Table 1. The comparison of the belly and scallop curves for the five leaflet designs (present: $D1^V$, $D2^U$ and past: $D3^U$, $D4^V$, $D5^U$) is presented in Fig. 1C and D. The thickness \mathcal{T} of newly designed leaflets, $D1^V$ and $D2^U$, is fixed at $300 \mu\text{m}$ in contrast to previous geometries whose leaflets were 500-micron-thick.

[Table 1 about here.]

2.1.3 Leaflet constitutive relationships and material parameters

Three constitutive material models are considered for the valve leaflets: synthetic elastomeric material (ELA), glutaraldehyde-pretreated bovine pericardial tissue (BOV) and porcine tissue (PORC). The six resulting valve configurations investigated in the present study are $D1^V$ -ELA, $D1^V$ -BOV, $D1^V$ -PORC, $D2^U$ -ELA, $D2^U$ -BOV and $D2^U$ -PORC. All material parameters are collected in Table 2.

The synthetic elastomeric (ELA) leaflets are modelled with an isotropic two-parameter Mooney-Rivlin constitutive law. The strain energy density reads:

$$W_{\text{ELA}} = C_{10}^{\text{MR}}(\bar{I}_1 - 3) + C_{01}^{\text{MR}}(\bar{I}_2 - 3), \quad (3)$$

where C_{10}^{MR} and C_{01}^{MR} are material constants and \bar{I}_1 , \bar{I}_2 are the first and second invariants of the deviatoric right Cauchy-Green deformation tensor. The two coefficients were fitted

to experimental uniaxial tensile measurements of a silicone-based elastomeric material used for 3D-printed prosthetic valve prototypes¹⁴. The fitted stress-stretch curve is displayed in Fig. 3A.

The bovine pericardial (BOV) leaflets are described by the Holzapfel-Gasser-Ogden (HGO) model²², which accounts for anisotropy through two families of collagen fibres embedded in an isotropic ground matrix. The strain energy density reads:

$$W_{\text{BOV}} = C_{10}^{\text{HGO}} (\bar{I}_1 - 3) + \frac{k_1}{2k_2} \sum_{i=1}^2 \left(e^{k_2 (\bar{I}_{4i} - 1)^2} - 1 \right), \quad (4)$$

where C_{10}^{HGO} characterises the neo-Hookean isotropic matrix response, k_1 and k_2 are fibre stiffness and stiffening parameters and \bar{I}_{4i} is the pseudo-invariant associated with the i -th fibre family direction. The Macaulay brackets $\langle \cdot \rangle$ ensure that fibres contribute only under tension. The two fibre families, assumed mechanically equivalent ($k_{11} = k_{12} = k_1$, $k_{21} = k_{22} = k_2$), are oriented symmetrically at angles $\pm\beta$ with respect to the circumferential direction $\mathbf{e}_{\text{circum}}$ (Fig. 3C). The four parameters were regressed by Auricchio *et al.*² to match biaxial tensile test data of glutaraldehyde-pretreated bovine pericardium²⁹ and subsequently adopted for FSI simulations in^{48,11,12}. The circumferential and axial stress-stretch curves are plotted in Fig. 3A (green solid and dashed lines). The anisotropy is pronounced: at a stretch of 1.2, the circumferential stress is roughly six times the axial stress.

Porcine aortic valve tissue (PORC) is modelled with the exponential form of the HGO framework (exp-HGO), which differs from Eq. (4) by adopting an exponential rather than polynomial expression for the isotropic ground matrix:

$$W_{\text{PORC}} = C_{10}^{\text{eHGO}} C_{01}^{\text{eHGO}} \left(e^{C_{01}^{\text{eHGO}} (\bar{I}_1 - 3)} - 1 \right) + \frac{C_2^{\text{eHGO}}}{2C_3^{\text{eHGO}}} \left(e^{C_3^{\text{eHGO}} \langle E_\alpha \rangle^2} - 1 \right), \quad (5)$$

with

$$E_\alpha = \kappa (\bar{I}_1 - 3) + (1 - 3\kappa) (\bar{I}_4 - 1), \quad (6)$$

where C_{10}^{eHGO} and C_{01}^{eHGO} govern the isotropic matrix response, C_2^{eHGO} and C_3^{eHGO} are fibre stiffness and stiffening parameters and κ is the fibre dispersion parameter. The single fibre family is oriented at θ with respect to the circumferential direction. The parameters were identified from the biaxial tensile test data reported by Laville *et al.*³⁰ for native

porcine aortic valve leaflets and by Murdock *et al.*³⁵ for porcine pericardium. In Fig. 3B, the exp-HGO stress-stretch curves used in the FSI simulations (red solid and dashed lines for circumferential and axial directions) are compared against these experimental datasets. Porcine tissue displays a more abrupt non-linear stiffening at relatively low stretches and a larger circumferential-to-axial stress ratio than bovine pericardium. At stretches above 1.1, its stiffness exceeds that of both bovine pericardium and the elastomeric material (Fig. 3A), a property that directly influences the leaflet dynamics and the ensuing haemodynamic environment throughout systole.

[Table 2 about here.]

[Figure 3 about here.]

2.2 Fluid-structure interaction (FSI) simulation setup

The computational domain and numerical setup are illustrated in Fig. 2. A patient-specific curved aorta geometry, encompassing the left ventricular outflow tract (LVOT), the sinus of Valsalva and the curved ascending aorta, is employed (Fig. 2A). These volumes are embedded into a rectilinear fluid grid (Fig. 2B). The physics of both fluid and structural sub-problems is synchronously solved and strongly coupled through a partitioned approach involving a modified and dedicated immersed boundary method^{36,11}.

The incompressible Navier-Stokes equations are solved on a fixed Cartesian grid of dimensions $55 \times 65 \times 110 \text{ mm}^3$ consisting of approximately 47 million grid points. The fluid solver uses high-order compact finite differences on staggered grids, an explicit third-order Runge-Kutta scheme for the advective term and a semi-implicit Crank-Nicolson scheme for the viscous term¹⁹. The pressure-velocity coupling is resolved through a Schur complement formulation with a commutation-based preconditioner and multigrid-accelerated iterative solvers^{19,36}. Periodic boundary conditions are prescribed at the borders of the Cartesian grid and cylindrical fringe regions are utilised to impose a prescribed pressure difference at

the inflow and outflow boundaries, following the methodology of Corso *et al.*¹¹. The forcing term within these cylindrical zones produces physiological systolic flow conditions, encompassing flow acceleration and deceleration, with a peak flow rate of approximately 25 L/min (inset of Fig. 2B). The Reynolds number at the valvular orifice Re_{orifice} attains values up to 8,000 during peak systole.

The elastodynamics equation for the structural sub-problem is solved on a tetrahedral mesh of approximately 280,000 first-order Galerkin finite elements using the Multiphysics Object-Oriented Simulation Environment (MOOSE) framework⁴³. The temporal integration relies on a second-order central difference scheme with implicit evaluation of the elastic residual³⁶. The Newton method linearises the system of non-linear equations and the resulting linear system is solved with a generalised minimal residual iterative method (GMRES) preconditioned by an additive Schwarz method^{43,3}. The strong coupling between the fluid and structural solvers is effected through a parallel variational transfer²⁶ of velocities (from fluid grid to solid mesh) and of reaction forces (from solid mesh to fluid grid). This transfer is based upon the resolution of L^2 -projection problems requiring the assembly of mortar-type matrices derived from the basis functions expressed on the overlapping mesh and grid points and for the Lagrange multiplier, as described in^{36,26}. The fluid and solid sub-problems are solved synchronously with a time-step of 2.5×10^{-6} s and an iterative procedure ensures velocity and force continuity at the fluid-structure interface until a relative tolerance of 10^{-6} is met^{36,11}.

For each of the six valve configurations, systole is simulated over a physical time of 0.25 s. Blood is modelled as a Newtonian fluid with kinematic viscosity $\nu_f = 3.77 \times 10^{-6}$ m²/s and density $\rho_f = 1,060$ kg/m³⁸. The aortic wall is treated as a nearly incompressible neo-Hookean material with a shear modulus of 380 kPa³⁷. The valve ring is described by a linear elastic constitutive relationship with a bulk modulus of 3 MPa and a shear modulus of 0.3 MPa¹¹. The hyperelastic leaflet material response is detailed in Section 2.1. The densities for the structural inertial terms are 1,100 kg/m³ for the crown and leaflets and 1,200 kg/m³ for the aorta wall. The solid incompressibility constraint is enforced through a penalty term with a

bulk modulus of 50 kPa^{11,37}. The reference velocity and length for the non-dimensionalisation of the Navier-Stokes equations are $\mathcal{U}_0 = 0.772$ m/s and $\mathcal{L}_0 = \mathcal{D} = 0.022$ m, from which the non-dimensional time is defined as $t^* = (\mathcal{U}_0/\mathcal{L}_0) \cdot t$.

2.3 Calcification-relevant field quantities at the leaflet

2.3.1 Finite-Time Lyapunov Exponents from leaflet deformation gradients

To characterise the kinematic coherence of Lagrangian material point trajectories on the leaflet, Finite-Time Lyapunov Exponents (FTLE) are computed from successive structural deformation gradients at each mesh node.

Consider the dynamical system governing the motion of a material point \mathbf{X} on the leaflet surface:

$$\frac{d\mathbf{x}}{dt} = \mathbf{v}(\mathbf{x}, t), \quad \mathbf{x}(t_0) = \mathbf{X}_0, \quad (7)$$

where $\mathbf{x}(t)$ denotes the position at time t and \mathbf{v} the leaflet surface velocity. The deformation map $\Phi_{t_0}^{t_0+T} : \mathbf{X}_0 \mapsto \mathbf{x}(t_0 + T)$ maps each material point from its reference position to its position at time $t_0 + T$. The associated deformation gradient tensor is $\mathbf{F}_{t_0}^{t_0+T} = \nabla_{\mathbf{X}} \Phi_{t_0}^{t_0+T} = \frac{\partial \mathbf{x}(t_0+T)}{\partial \mathbf{X}_0}$.

An incremental formulation is adopted in this work. The incremental deformation gradient between time instants t_n and t_{n+1} is $\mathbf{f}_n^{n+1} = \nabla_{\mathbf{x}(t_n)} \Phi_{t_n}^{t_{n+1}} = \mathbf{F}_{t_0}^{t_{n+1}} [\mathbf{F}_{t_0}^{t_n}]^{-1}$ and the total deformation gradient over $N = \frac{T}{\Delta t}$ increments is obtained by composition:

$$\mathbf{F}_{t_0}^{t_0+T} = \mathbf{f}_{N-1}^N \cdot \mathbf{f}_{N-2}^{N-1} \cdots \mathbf{f}_1^2 \cdot \mathbf{f}_0^1. \quad (8)$$

The incremental right Cauchy-Green strain tensor is:

$$\mathbf{C}_{\text{inc}}(t_n, t_{n+1}) = \left[(\mathbf{F}_{t_0}^{t_n})^{-1} \right]^T \left[\mathbf{F}_{t_0}^{t_{n+1}} \right]^T \mathbf{F}_{t_0}^{t_{n+1}} (\mathbf{F}_{t_0}^{t_n})^{-1} \quad (9)$$

The incremental FTLE is then defined as:

$$\text{FTLE}(t_n, t_{n+1}) = \frac{1}{\Delta t} \ln \left(\sqrt{\lambda_{\max}(\mathbf{C}_{\text{inc}})} \right), \quad (10)$$

where $\lambda_{\max}(\mathbf{C}_{\text{inc}})$ is the largest eigenvalue of \mathbf{C}_{inc} . The FTLE thus represents the maximal exponential rate of separation between infinitesimally close material points over the interval $t_{n+1} - t_n = \Delta t = 1$ ms. The total time interval T over which the incremental FTLE is computed is equal to 0.23 s after discarding the initial time instants involving the opening of the valve leaflets. Elevated FTLE values identify regions of heterogeneous surface expansion, where diverging material point trajectories enlarge the leaflet area available for contact with calcium phosphate species circulating in the surrounding fluid. It is hypothesised that such conditions favour preferential mineral nucleation at these sites.

2.3.2 Wall shear stress at the leaflet surfaces

The wall shear stress vector at the ventricular side of the leaflets is computed from the fluid velocity field at the fluid-structure interface. For an incompressible Newtonian fluid, the WSS vector is^{48,10}:

$$\mathbf{WSS} = 2\mu \mathbf{S} \cdot \mathbf{n}, \quad (11)$$

where $\mu = 0.004$ Pa·s is the dynamic viscosity of blood, $\mathbf{S} = 1/2 (\nabla \mathbf{u} + \nabla \mathbf{u}^T)$ is the rate-of-strain tensor (with diagonal entries set to zero to exclude spurious normal stresses), \mathbf{u} is the flow velocity and \mathbf{n} is the unit outward normal to the leaflet surface. The Euclidean norm $\|\mathbf{WSS}\|$ is evaluated at each mesh node and at time instants 1 ms apart throughout systole. Two temporal features are extracted from the time-dependent WSS magnitude field: the time-averaged WSS magnitude (TAWSS) and the temporal standard deviation of $\|\mathbf{WSS}\|$. The latter quantifies the temporal variability of the shear loading at each location and has been related to regions susceptible to endothelial damage and mineral nucleation^{48,10}.

2.4 Unsupervised k -means classification of calcification risk

An unsupervised classification framework based on the k -means clustering algorithm³¹ is proposed to stratify the leaflet surface into regions of distinct calcification risk. The key advantage over regression-based methods⁴⁸ is that no coefficient fitting to experimental calcification data is required. Two separate classifications are performed, one from FTLE-derived

features and one from WSS-derived features. The number of time steps used to extract the temporal statistical features is 230.

2.4.1 Feature vectors

For the FTLE-based classification, the feature vector at each mesh node i consists of two entries: (1) the temporal minimum of the FTLE, $\text{FTLE}_{\min}^{(i)}$, and (2) the Euclidean norm of the spatial gradient of the temporal-minimum FTLE, $\|\nabla \text{FTLE}_{\min}^{(i)}\|$. The temporal minimum of the FTLE field is retained, as it isolates regions of sustained trajectory incoherence throughout systole; the attendant heterogeneous surface expansion at these sites increases the leaflet area exposed to calcium phosphate species in the surrounding fluid, fostering preferential mineral nucleation and deposition.

For the WSS-based classification, the feature vector at each node i comprises three entries: (1) the temporal mean of $\|\mathbf{WSS}\|$, (2) the temporal standard deviation of $\|\mathbf{WSS}\|$ and (3) the Euclidean norm of the spatial gradient of the temporal standard deviation of $\|\mathbf{WSS}\|$. Spatial gradients are estimated via finite differences over a local neighbourhood of radius 1 mm centred at each node.

2.4.2 Standardisation and clustering

Prior to clustering, each feature is standardised through a quantile transform to a uniform distribution. The number of quantiles equals the number of leaflet surface nodes divided by 10, i.e. about 400 for each valve configuration. This non-linear transformation removes skewness and renders the classification robust to outliers⁴². The standardised features are then combined into a weighted feature vector, with a weight of 0.75 attributed to the physical quantity (temporal-minimum FTLE or temporal mean and standard deviation of WSS) and 0.25 to the spatial gradient term. The k -means algorithm, minimising squared differences between the mean value $\boldsymbol{\mu}_k$ of the cluster \mathcal{C}_k and the features' value within the cluster (Eq. 12), is applied with $K = 4$ clusters, confirmed as optimal via silhouette analysis (see

Fig. S1 in the Supporting Information (SI)).

$$\min_{\{\boldsymbol{\mu}_k\}_{k=1}^K} \sum_{k=1}^K \sum_{i \in \mathcal{C}_k} \|\mathbf{x}_i - \boldsymbol{\mu}_k\|^2, \quad (12)$$

with \mathbf{x}_i , the standardised and combined feature vector (temporal-minimum FTLE or temporal mean and standard deviation of WSS). The four clusters are reordered by ascending spatially averaged physical quantity (temporal-minimum FTLE for the FTLE-based analysis, mean $\|\mathbf{WSS}\|$ for the WSS-based analysis) and labelled: low, medium-low, medium-high and high calcification risk.

2.4.3 Risk score

A scalar risk score RS is defined as a weighted sum of the percentage of mesh nodes belonging to each cluster:

$$RS = w_1 \cdot P_{\text{low}} + w_2 \cdot P_{\text{med-low}} + w_3 \cdot P_{\text{med-high}} + w_4 \cdot P_{\text{high}}, \quad (13)$$

where P_k is the percentage of nodes in cluster k and w_k the associated weight. The weights are calibrated so that the risk scores for the bovine pericardial configurations fall within the range of calcification area percentages observed experimentally in Tsolaki, Corso *et al.*⁴⁸ (11.7-55.4% for the combined FTLE- and WSS-based RS in the present study against 18-51% observed out of explanted bovine pericardial valves in⁴⁸). The weights are [$w_1 = 0.0$; $w_2 = 0.1$; $w_3 = 0.4$; $w_4 = 1.0$].

3 Results and Discussion

The results are presented in six parts. Section 3.1 examines the leaflet opening dynamics and flutter characteristics for all six configurations throughout systole. Section 3.2 describes the instantaneous WSS distributions on the ventricular leaflet surface at five systolic time instants. The FTLE- and WSS-based k -means risk clusters are presented in Sections 3.3 and 3.4, respectively; the temporal features of both fields serving as inputs to the classification are discussed in the Supporting Information (Figs S3 and S4). Section 3.5 validates

the unsupervised clustering against the experimentally calibrated calcification intensity of Tsolaki, Corso *et al.*⁴⁸ for the two bovine pericardial configurations. Section 3.6 closes with a comprehensive risk ranking of the six valve designs across both descriptors.

3.1 Leaflet motion analysis

Figure 4 presents the spatially averaged displacement magnitude of the leaflet mesh nodes (averaged over all three leaflets) relative to the initial position at $t = 0$ s for each geometry and material combination. This metric condenses the opening dynamics, flutter characteristics and flapping behaviour into a single time-resolved signal. Videos of the complete leaflet motion throughout systole for all six valve configurations accompany this article in Supporting Information (Video V1). The flutter and flapping characteristics of all six valve configurations are compiled in Table 3 for ease of comparison.

D1^V geometry. Among the three D1^V configurations, the porcine tissue leaflets open most rapidly, displaying the steepest initial slope up to $t \approx 0.026$ s (Fig. 4A), with the bovine pericardial leaflets following closely and the elastomeric leaflets being the slowest to reach their fully open position. Inspection of the leaflet motion video (Video V1 in SI) reveals that, for D1^V-ELA, two of the three cusps attain their open configuration by $t \approx 0.04$ s while the third requires approximately double the time ($t \approx 0.08$ s), producing a transiently asymmetric orifice. The D1^V-PORC curve exhibits a pronounced peak of approximately 2.5 mm near $t \approx 0.05$ s (red curve in Fig. 4A). Examination of the leaflet motion video demonstrates that by $t \approx 0.05$ s the orifice, for the D1^V-PORC case, has already begun to contract, indicating that the peak does not originate from an inertial overshoot of the leaflets beyond their equilibrium open position. Rather, the porcine leaflets produce the largest effective orifice area of the three D1^V configurations and a correspondingly intense systolic jet whose impingement displaces the compliant aortic wall. This wall motion propagates through the crown and then to the leaflet attachment with a short phase lag, so that the rigid-body shift of the valve ring reaches its maximum after the leaflets have already started to recoil. The spatially averaged displacement magnitude, being measured from the initial

417 leaflet position at $t = 0$ s, therefore reflects this superimposed crown translation. The effect
 418 is considerably weaker for D1^V-BOV and D1^V-ELA, whose smaller orifice areas attenuate
 419 the jet impingement on the aortic wall.

420 During mid-to-late systole, the three materials give rise to markedly different dynamic
 421 regimes. The D1^V-PORC leaflets undergo low-frequency flapping between $t = 0.134$ and
 422 0.20 s at approximately 45 Hz with a displacement magnitude amplitude of roughly 2 mm
 423 (Fig. 4A, red curve). The pronounced anisotropy of porcine tissue, characterised by a steep
 424 circumferential stiffening and a considerably softer axial response at physiological stretches
 425 (circumferential-to-axial stiffness ratio exceeding 3:1 at stretch $\lambda = 1.1$; cf. Fig. 3A), likely
 426 favours preferential deformation modes that sustain this large-amplitude oscillation. The
 427 D1^V-BOV leaflets instead present a higher-frequency flutter between $t = 0.037$ and 0.055 s
 428 and between $t = 0.092$ and 0.11 s at roughly 330 Hz with a reduced amplitude of about
 429 0.4 mm, followed by a lower-frequency flapping episode (≈ 55 Hz, amplitude ≈ 1 mm) be-
 430 tween $t = 0.12$ and 0.20 s (Fig. 4A, green curve). This dual-mode behaviour shares char-
 431 acteristics with the flutter reported for bovine pericardial valves in our prior works^{48,11}.
 432 Indeed, the D3^U leaflet geometry (see Table 1) exhibited axisymmetric periodic flutter with
 433 displacement magnitudes up to 1.2 mm. The D1^V-ELA leaflets, by contrast, remain largely
 434 stable after opening and are less susceptible to pronounced flutter apart from intermittent
 435 single-leaflet oscillations (Fig. 4A, ochre curve). This relative stability is consistent with the
 436 higher isotropic flexural stiffness of the elastomeric material (see Section 2.1 and Fig. 3A),
 437 which confers greater resistance to the bending-dominated oscillatory modes about the cir-
 438 cumferential axis exhibited by both biological tissues, in line with the primary role of flexural
 439 stiffness in governing leaflet flutter identified by Johnson *et al.*^{23,24}. In a systematic computa-
 440 tional study, Johnson *et al.*²³ showed that reducing bovine pericardial leaflet thickness from
 441 0.386 mm to 50% of this value introduced a narrow-band flutter centred around 50 Hz whose
 442 signal energy exceeded the baseline by more than an order of magnitude, with a further re-
 443 duction to 25% broadening the spectrum to 20-60 Hz; a follow-up investigation²⁴ attributed
 444 this behaviour primarily to the reduction in flexural stiffness rather than membrane stiffness.

Within the present study, all three materials share the same 300 μm leaflet thickness, so the lower effective bending rigidity of BOV and PORC relative to ELA stems from their lower axial modulus at physiological stretches (Fig. 3A), consistently producing the more intense flutter observed in both biological tissue configurations. The higher 330 Hz flutter frequency of D1^V-BOV compared with the axisymmetric periodic flutter (displacement magnitudes up to 1.2 mm) reported for the D3^U geometry^{48,11}, which used 500 μm thick leaflets, may reflect the combined influence of the reduced leaflet thickness and the patient-specific curved aorta geometry adopted here.

D2^U geometry. For the D2^U geometry, the porcine tissue leaflets again open fastest, but the second-fastest are now the elastomeric leaflets rather than the bovine pericardial ones (Fig. 4B). As with D1^V-PORC, the D2^U-PORC curve features a transient peak (≈ 2.3 mm near $t \approx 0.05$ s) arising from the same jet-impingement-induced wall and crown displacement mechanism, again occurring after the orifice has begun contracting (Fig. 4B, red curve). In contrast to the D1^V case, the D2^U-ELA leaflets open symmetrically amongst the three cusps (see Video V1 in SI). The D2^U-BOV leaflets are the slowest to open, a behaviour analogous to the stable D5^U design (see Table 1) reported in our prior studies^{11,12}. Remarkably, the D2^U-BOV leaflets exhibit no discernible high-frequency or low-frequency flutter throughout the entirety of systole, rendering them the most dynamically stable configuration among the six cases investigated (Fig. 4B, green curve). This exceptional stability likely stems from the broad U-shaped scallop profile, which constrains leaflet excursion and distributes the haemodynamic loading more uniformly. The D2^U-PORC leaflets undergo low-frequency flapping between $t = 0.127$ and 0.21 s at approximately 45 Hz, matching the flapping frequency of the D1^V-PORC case albeit with a reduced displacement amplitude of roughly 1 mm (Fig. 4B, red curve). Examination of the leaflet motion video (Video V1 in SI) reveals that two of the three porcine leaflets for D2^U are animated by stronger flutter than the third, recalling the asymmetric bi-directional flutter noted for the D4^V leaflet geometry (Table 1 in^{48,11}). The D2^U-ELA leaflets are characterised by sustained flutter over a broad interval ($t = 0.068$ -0.19 s) at frequencies between 45 and 60 Hz with reduced amplitudes

of 0.6-0.8 mm (Fig. 4B, ochre curve), the motion remaining rather symmetric amongst the three cusps. The D2^U-ELA flutter is less intense than that of D2^U-PORC but stronger and more sustained than that noted for D2^U-BOV, which underscores the material-geometry interdependence governing flutter suppression.

Taken together, these observations confirm that leaflet material properties and scallop geometry jointly govern the flutter regime. Porcine tissue, despite sustaining the highest circumferential stresses of the three materials at stretches $\lambda > 1.1$ (cf. Fig. 3A), promotes low-frequency high-amplitude flapping in both geometries, a behaviour driven by its pronounced mechanical anisotropy (circumferential-to-axial stiffness ratio exceeding 3:1 at $\lambda = 1.1$). Bovine pericardium can either sustain high-frequency low-amplitude flutter (D1^V) or suppress flutter entirely (D2^U) depending on the scallop profile. The elastomeric material occupies an intermediate position, with its dynamic response modulated strongly by the leaflet geometry. Given the established connection between flutter-induced cyclic strain and accelerated structural degeneration^{48,23,24,17,13}, these differences in dynamic behaviour are expected to translate into distinct calcification risk profiles, explored through the FTLE and WSS clustering analysis in the subsequent sections. Table 3 summarises the leaflet motion characteristics pertaining to the presence or absence of flutter for the six valve configurations.

[Figure 4 about here.]

[Table 3 about here.]

3.2 Wall shear stress fields during systole

The instantaneous WSS magnitude distributions on the ventricular side of the leaflets are presented for all six configurations in Fig. 5, covering five time instants during systole ($t = 0.05, 0.10, 0.15, 0.20$ and 0.25 s); streamlines coloured by velocity magnitude are superimposed to illustrate the near-valve flow patterns. The spatially maximum and spatially averaged WSS magnitude over the full systolic interval are provided in Fig. S2 of SI for all

configurations. The reader is referred to Fig. 2A for the nomenclature of the different regions of the leaflet.

Early systole ($t = 0.05$ s). At the onset of systole the leaflets are still approaching their fully open position. For D1^V, the BOV and PORC configurations already exhibit comparable and elevated spatially averaged WSS (≈ 1.5 Pa; Fig. S2C), consistent with their faster opening relative to ELA (Section 3.1). D1^V-ELA lags markedly (with a spatially averaged WSS ≈ 1.0 Pa; Fig. S2C) owing to its slower and asymmetric leaflet opening. For D2^U, BOV and PORC display lower WSS than their D1^V counterparts, whereas D2^U-ELA already reaches a spatially averaged WSS comparable to D2^U-PORC (≈ 1.4 Pa; Fig. S2D), reflecting the more symmetric and rapid opening of the elastomeric leaflets on this geometry (Section 3.1). D2^U-BOV presents the least shear at the leaflet wall of all six configurations at this instant.

Acceleration to peak systole ($t = 0.10$ s). As the flow rate rises, the systolic jet strengthens and WSS levels increase across all configurations. For D1^V-BOV and D1^V-ELA, elevated WSS extends from the free edge towards the central belly and along the attachment curve near the commissures (Fig. 5A and B), a spatial pattern consistent with the TAWSS distribution reported in⁴⁸ for bovine pericardial leaflets. In fact, the narrow gap between each leaflet and the crown promotes intense shear through confinement of recirculating blood in the sinus. D1^V-PORC, with its wider orifice, distributes WSS more broadly across the belly at reduced peak magnitudes (Fig. 5C). For D2^U, D2^U-BOV remains the lowest-WSS case with shear confined to narrow bands at the free edge and commissures (Fig. 5B), whilst D2^U-PORC and D2^U-ELA present moderate belly WSS (Fig. 5A and C).

Peak and mid-systole ($t = 0.15$ - 0.20 s). The maximum streamline velocity reaches $U_{\max} = 2.0$ m/s and the coupling between leaflet flutter and the WSS field becomes apparent. For D1^V, the spatially averaged WSS peaks at ≈ 3.0 Pa for ELA and ≈ 2.5 Pa for BOV (Fig. S2C), both sustained by narrow, concentrated jets. D1^V-ELA, whose leaflets remain largely quiescent after opening, presents a comparatively smooth WSS distribution spread across the belly (Fig. 5A). D1^V-BOV displays a noticeably patchy WSS field between

$t = 0.15$ and 0.20 s, reflecting the 55 Hz flapping documented in Section 3.1. D1^V-PORC records the lowest spatially averaged WSS of the three D1^V configurations at this stage (≈ 2.5 Pa; Fig. S2C): its wide orifice diffuses the jet and attenuates mean shear, yet the 45 Hz flapping (Table 3) generates spatially irregular high-WSS patches that shift position over time (Fig. 5C). For D2^U, D2^U-ELA reaches the highest spatially averaged WSS (≈ 2.7 Pa; Fig. S2D), with sustained 45-60 Hz flutter (see Table 3) producing broad, heterogeneous shear patterns across the belly (Fig. 5A). D2^U-PORC exhibits pronounced instantaneous WSS peaks (up to ≈ 25 -30 Pa; Fig. S2B) driven by its 45 Hz flapping (see Table 3), whilst the spatially averaged value remains moderate (≈ 2 Pa; Fig. S2D). D2^U-BOV stands out as the most temporally stable case, with persistently low belly shear and elevated values confined to the free edge and commissural attachment (Fig. 5B).

Late systole ($t = 0.25$ s). During deceleration, the jet breaks down into disordered, low-velocity streamlines and WSS magnitudes fall below 1 Pa over most of the belly surface for all configurations. Residual shear concentrates near the free edge and commissural attachment, where recirculating flow in the sinus sustains non-negligible velocity gradients. D2^U-BOV exhibits the most striking contrast at this instant: one leaflet has already begun closing and the belly is almost entirely at near-zero WSS. Configurations that underwent flutter during peak systole retain slightly higher and more spatially heterogeneous residual WSS than the quiescent cases.

In summary, the ventricular-side WSS field is jointly governed by the orifice geometry, which sets the jet width and velocity, and by the leaflet dynamics, which modulate its spatial footprint over time. D2^U-BOV consistently presents the lowest WSS across all time instants. Amongst the D1^V configurations, D1^V-PORC generates the most broadly distributed belly WSS at reduced peak magnitudes (Fig. 5C) whilst D1^V-ELA and D1^V-BOV sustain the highest spatially averaged WSS during peak systole (Fig. S2C). The free edge and commissural attachment sustain the highest instantaneous shear throughout systole, in agreement with the TAWSS distributions reported in⁴⁸. The central belly, by contrast, is characterised by low instantaneous WSS, a condition conducive to prolonged residence time and elevated

oscillatory shear index. As demonstrated in⁴⁸, these zones of low shear and high residence time coincide with the sites of preferential mineral accumulation observed in explanted bio-prosthetic valves. The influence of the distinct flutter regimes on the time-integrated WSS-derived indicators is quantified through the clustering framework in Section 3.4.

[Figure 5 about here.]

3.3 FTLE-based calcification risk clusters

The spatial distributions of the four k -means clusters obtained from the FTLE-derived feature vectors are displayed in Fig. 6 for the three leaflets of each valve configuration. The clusters are colour-coded as green (low risk), purple (medium-low risk), orange (medium-high risk) and red (high risk). The per-leaflet risk score RS^{FTLE} is indicated below each leaflet. For D2^U-BOV, the leaflet surfaces are predominantly occupied by low and medium-low risk clusters, with minimal occurrence of medium-high or high-risk regions. The risk scores across the three leaflets are 11.5%, 9.5% and 11.1%, rendering D2^U-BOV the configuration with the lowest FTLE-based calcification risk. D1^V-ELA shows moderately higher risk scores (16.2%, 13.1% and 14.4%), with small patches of medium-high risk appearing in the upper belly. D2^U-ELA presents risk scores of 21%, 22.2% and 18.3%, with medium-high and occasional high-risk clusters distributed across the belly. These clusters are more spatially concentrated than in D1^V-ELA, reflecting the distinct leaflet dynamics associated with the D2^U geometry. For D1^V-BOV, the risk scores rise to 28.9%, 24.9% and 30%, with the high-risk cluster occupying limited but discernible zones near the free edge and in the belly centre. The two porcine configurations exhibit the highest FTLE-based calcification risk. D1^V-PORC shows risk scores of 27%, 21% and 47.7%, with substantial portions of the belly classified as medium-high. D2^U-PORC presents the most adverse risk profile, with risk scores of 44.5%, 37% and 56.5%. In this configuration, the high and medium-high risk clusters cover a major fraction of the leaflet surface (concentrated in the belly and free edge regions), consistent with the elevated temporal-minimum FTLE values observed in Fig. S3 of SI.

[Figure 6 about here.]

3.4 WSS-based calcification risk clusters

Figure 7 presents the WSS-based k -means risk clusters RS^{WSS} for the six valve configurations, following the same colour coding and labelling convention as in Section 3.3.

The WSS-based clustering yields spatial patterns distinct from those of the FTLE-based clustering. The high-risk cluster (red) is more prominently situated in the belly centre, where the combination of low TAWSS and elevated temporal variability produces the most adverse haemodynamic conditions for the tissue. Compared with the FTLE-based analysis, the WSS-based risk scores are systematically higher for all configurations except D2^U-PORC, indicating that the haemodynamic shear environment penalises most valve designs more severely than the structural strain environment captured by the FTLE.

D2^U-BOV retains the lowest risk scores RS^{WSS} across both descriptors (16.2%, 13.9% and 17.2%), confirming the favourable biomechanical and haemodynamic environment associated with this configuration. D2^U-PORC presents WSS-based risk scores of 24.8%, 32.9% and 45%, placing it second in the WSS-based ranking despite occupying the highest position in the FTLE-based one. This reversal suggests that, for the porcine material with the D2^U geometry, the structural strain, as quantified by the FTLE-derived material point separation rate, is a stronger contributor to calcification risk than the haemodynamic shear field. D1^V-PORC exhibits WSS-based risk scores of 39.7%, 42.5% and 50.5%, which are comparable to or higher than its FTLE-based counterparts (27%, 21% and 47.7%), indicating a more balanced contribution from both descriptors for this geometry.

The two elastomeric configurations rank among the highest in WSS-based risk. D1^V-ELA shows tightly grouped scores of 47.8%, 47.1% and 49.2% (Fig. 7), markedly elevated compared with its FTLE-based values (16.2%, 13.1% and 14.4%, see Fig. 6). D2^U-ELA presents the highest overall WSS-based risk (52.7%, 50.9% and 58.2%), contrasting with its intermediate FTLE-based position. This behaviour can be attributed to the isotropic nature of the elastomer, which distributes strain uniformly across the leaflet surface yet generates intense

WSS fluctuations through larger jet velocities and subsequent systolic flow disturbances (see Fig. 5A). D1^V-BOV exhibits WSS-based risk scores of 42.8%, 44.8% and 63.1%, with L3 reaching the single highest per-leaflet value across all configurations. The pronounced inter-leaflet variability in D1^V-BOV, already observed in the FTLE-based analysis, is thus amplified in the WSS-based clustering.

A notable cross-cutting trend is the systematic elevation of both RS^{FTLE} and RS^{WSS} for leaflet L3 relative to L1 and L2. In the WSS-based analysis, this holds for all six configurations. In the FTLE-based analysis, it is particularly pronounced for the three configurations with the highest overall risk (D2^U-PORC, D1^V-PORC and D1^V-BOV), where the L3 risk score exceeds those of L1 and L2 by a wide margin. Leaflet L3 is seated in the sinus of Val-salva aligned with the inner (concave) aortic wall, which has the smaller radius of curvature. The curvature-induced asymmetry of the flow in the ascending aorta, whereby the systolic jet is deflected towards the outer wall and a secondary retrograde motion develops along the inner wall^{11,10}, produces an asymmetric haemodynamic loading on the three sinuses. The sinus facing the inner wall receives a less uniform washout and is exposed to lower and more oscillatory wall shear stress, both of which are established promoters of leaflet calcification. This aorta-geometry-driven mechanism operates independently of the leaflet material and geometry, underscoring the importance of patient-specific aortic anatomy in calcification risk prediction.

[Figure 7 about here.]

3.5 Validation against experimentally calibrated calcification data

The unsupervised k -means clustering of FTLE- and WSS-derived fields was validated against the experimentally calibrated calcification intensity of Tsolaki, Corso *et al.*⁴⁸, in which a power-law regression was fitted to micro-CT-derived calcification maps of explanted bovine pericardial valves, resulting in the following reconstructed intensity:

$$f_{\text{calcIrecon}} = C_1 \text{TSVI}_{d,\text{Ao}}^{C_2} + C_3 \text{TAWSS}_{d,\text{Ven}}^{C_4} + C_5 \text{SS}_{d,\text{Ao}}^{C_6}, \quad (14)$$

where the subscripts d denote normalised distributions, Ao and Ven refer to the aortic and ventricular sides of the leaflets respectively, TSVI is the topological shear variation index, TAWSS is the time-averaged wall shear stress magnitude, SS is the scalar strain and C_1 - C_6 are the fitted coefficients (Table S2 in⁴⁸). A sensitivity analysis in⁴⁸ showed that the TAWSS term on the ventricular side and the TSVI term on the aortic side account for approximately 65.5% and 44.5% of the reconstructed intensity respectively as independent contributions in this nonlinear additive model, the scalar strain term being negligible. The regression achieved a coefficient of determination $R^2 = 0.74$ on the testing dataset. The calcification intensity field was computed from Eq. (14) using the FSI-derived TSVI, TAWSS and SS fields for the D1^V-BOV and D2^U-BOV configurations, the only two for which the calibrated relationship of⁴⁸ is applicable since both employ bovine pericardial tissue.

The Spearman rank correlation coefficient ρ_S served as the primary validation metric. It measures the monotonic spatial agreement between two variables by correlating their rank orderings, thereby quantifying how faithfully the cluster-derived risk map reproduces the spatial pattern of the continuous calcification intensity field (first column of Fig. 8) without requiring any discretisation or threshold calibration. Fig. 8 presents the comparison for D1^V-BOV. The first column shows the reference risk levels from the calcification intensity field (Eq. 14) partitioned into quartiles; the second and third columns display the FTLE- and WSS-based cluster maps; the fourth column presents their arithmetic mean. Neither descriptor alone faithfully reproduces the spatial calcification intensity pattern. The FTLE-based map ($\rho_S = 0.79$) captures the high-risk zone in the central belly but overestimates the low-risk area near the commissures and attachment curve. The WSS-based map ($\rho_S = 0.82$) delineates the belly risk region more prominently yet assigns excessively uniform medium-high to high risk across the belly of L2 and L3, blurring the gradation towards the low-risk periphery. Tellingly, these complementary shortcomings cancel when the two descriptors are combined. In fact, the arithmetic mean of the FTLE and WSS cluster indices achieves $\rho_S = 0.975$, reproducing the four-tier spatial risk pattern of the calcification intensity field (Eq. (14) and first column of Fig. 8) with high fidelity across all three leaflets (see fourth

column of Fig. 8). For D2^U-BOV, the same trend holds at a lower level, with individual correlations of $\rho_S = 0.63$ (FTLE) and 0.60 (WSS) rising to $\rho_S = 0.86$ for the arithmetic mean.

To verify that the strong monotonic association translates into correct ordinal classification, the continuous calcification intensity field was discretised into four balanced quartile classes and a combined risk score $S = w \cdot \text{FTLE}_{\text{cluster}} + (1 - w) \cdot \text{WSS}_{\text{cluster}}$ was optimised against these classes using Cohen’s weighted kappa κ_w , which measures ordinal agreement between two classification schemes whilst penalising disagreements proportionally to their distance from the diagonal. The optimisation converged to $w = 0.51$ for both geometries, confirming an approximately equal contribution of the two descriptors. The resulting κ_w values of 0.911 for D1^V-BOV and 0.724 for D2^U-BOV correspond to near-perfect and substantial ordinal agreement respectively on the Landis and Koch scale²⁸. For D1^V-BOV, 88.6% of mesh nodes fell into the correct calcification intensity quartile and all misclassifications were confined to adjacent classes.

These results establish that the unsupervised clustering framework, when combining FTLE and WSS information, reproduces the calcification risk stratification of⁴⁸ without itself requiring any fitting to experimental data. The near-equal optimal weight ($w \approx 0.50$) and its consistency across both geometries reinforce the conclusion of the comprehensive risk analysis (Section 3.6): leaflet material point separation and haemodynamic wall shear stress are co-dependent and approximately equally weighted drivers of bioprosthetic valve calcification.

[Figure 8 about here.]

3.6 Comprehensive valve design risk analysis

Fig. 9A and B present the overall risk scores RS^{FTLE} and RS^{WSS} for all six configurations. The corresponding proportions of high-risk nodes on the leaflet surface and per-cluster breakdowns across all four risk categories are provided in Fig. S5 of the SI.

3.6.1 FTLE-based risk ranking

The FTLE-based clustering, constructed from the temporal-minimum FTLE and its spatial gradients, quantifies the spatial coherence of leaflet material points throughout systole (Fig. 9A). Ranked by increasing RS^{FTLE} , the six configurations are: D2^U-BOV (10.7%), D1^V-ELA (14.8%), D2^U-ELA (20.5%), D1^V-BOV (27.9%), D1^V-PORC (31.9%) and D2^U-PORC (46.0%). The high-risk surface fraction spans from 0.9% for D2^U-BOV to 30.9% for D2^U-PORC (Fig. S5A). The breakdown of leaflet surface nodes across the four risk categories (Fig. S5B) corroborates this trend: D2^U-BOV is dominated by low and medium-low risk whereas D2^U-PORC is overwhelmingly composed of medium-high and high risk zones. This ranking is governed chiefly by the constitutive response of the leaflet material. Porcine tissue, the most anisotropic of the three (circumferential-to-axial stiffness ratio exceeding 3:1 at stretch $\lambda = 1.1$), channels deformation into preferential directions and generates localised high-strain regions that translate into elevated FTLE values and steep spatial gradients, placing both PORC configurations at the bottom of the ranking irrespective of geometry. The isotropic elastomer distributes strain more uniformly across the leaflet surface, producing low FTLE magnitudes and modest spatial gradients; both ELA configurations therefore occupy favourable positions (D1^V-ELA second, D2^U-ELA third). Bovine pericardium sits between these extremes. In fact, its moderate anisotropy produces intermediate FTLE levels for the D1^V geometry ($RS^{\text{FTLE}} = 27.9\%$) but, when paired with the constraining D2^U scallop profile that curbs leaflet excursion and strain localisation, delivers the lowest overall RS^{FTLE} (10.7%) as shown in Fig. 9A.

3.6.2 WSS-based risk ranking

The WSS-based ranking (Fig. 9B) gives a different ordering: D2^U-BOV (15.8%), D2^U-PORC (34.2%), D1^V-PORC (44.2%), D1^V-ELA (48.0%), D1^V-BOV (50.2%) and D2^U-ELA (53.9%). D2^U-BOV again emerges as the best-performing configuration, with only 6.4% of its leaflet surfaces classified as high risk (Fig. S5C) and a risk breakdown dominated by the low-risk category (Fig. S5D). The three highest- RS^{WSS} configurations (D1^V-ELA, D1^V-BOV and

712 D2^U-ELA) are those exhibiting narrower leaflet opening (see Fig. 5A and B), sustained
 713 flutter (Table 3) or both, which raise the mean WSS and its temporal variability across
 714 the leaflet surface. D1^V-BOV warrants a brief remark: its high-risk surface fraction (34.9%,
 715 Fig. S5C) is slightly lower than that of D1^V-ELA (38.7%), yet its overall RS^{WSS} is marginally
 716 higher (50.2% versus 48.0%) because a broader spread of medium-high risk nodes inflates
 717 the composite score (Eq. 13, Fig. S5D). D1^V configurations generally rank worse than their
 718 D2^U counterparts, consistent with the systematically higher instantaneous and fluctuating
 719 WSS magnitudes recorded on D1^V leaflets throughout systole (Section 3.2 and Fig. S4).

720 **3.6.3 Combined interpretation**

721 The two rankings are complementary rather than redundant. The FTLE-based analysis pe-
 722 nalisises configurations that concentrate strain into localised high-gradient zones (both PORC
 723 cases) whereas the WSS-based analysis penalises those sustaining intense mean shear through
 724 narrow orifices (D1^V-ELA, D1^V-BOV) or elevated temporal shear variability through persis-
 725 tent flutter (D2^U-ELA). Two cases illustrate the disparity most sharply. D2^U-PORC ranks
 726 last in the FTLE-based analysis ($RS^{FTLE} = 46.0\%$, Fig. 9A) yet second-best in the WSS-
 727 based one ($RS^{WSS} = 34.2\%$, Fig. 9B): the stiff anisotropic porcine tissue restricts leaflet
 728 excursion and moderates shear variability, whilst the tissue itself undergoes severe strain
 729 localisation driving elevated material point separation rates. Conversely, D2^U-ELA ranks
 730 third-best for FTLE ($RS^{FTLE} = 20.5\%$) yet worst for WSS ($RS^{WSS} = 53.9\%$): the isotropic
 731 elastomer distributes strain uniformly, yet its sustained 45-60 Hz flutter (see Section 3.1 and
 732 Table 3) produces the highest temporal shear variability of all six configurations.

733 The validation reported in Section 3.5 demonstrates that neither indicator alone reproduces
 734 the calcification risk predicted by the experimentally calibrated relationship of Tsolaki, Corso
 735 *et al.*⁴⁸. The arithmetic mean of the FTLE- and WSS-based risk classifications best matches
 736 that risk stratification, confirming that leaflet material point separation quantified with
 737 FTLE and haemodynamic wall shear stress act as co-dependent drivers of calcific degenera-
 738 tion.

D2^U-BOV is the sole configuration that ranks first in both analyses ($RS^{\text{FTLE}} = 10.7\%$ in Fig. 9A, $RS^{\text{WSS}} = 15.8\%$ in Fig. 9B). The combination of the D2^U leaflet geometry (broader U-shaped scallop) and bovine pericardial tissue furnishes the most favourable biomechanical and haemodynamic environment for long-term durability: the constraining scallop suppresses flutter, limits strain localisation and keeps WSS variability low. This conclusion is consonant with our prior studies^{11,12}, where the D5^U (Table 1, U-shaped scallop, same family as D2^U) promoted a more organised flow, lower drag and reduced kinetic energy anisotropy. From a translational standpoint, pairing porcine tissue with the D2^U leaflet geometry may offer acceptable haemodynamic performance yet expose the tissue to severe structural loading and therefore accelerated calcification, whereas an isotropic elastomeric material delivers favourable strain homogeneity at the cost of elevated shear at the leaflet surface. Accounting for both risk dimensions simultaneously is therefore a fundamental design principle for next-generation prosthetic valve optimisation.

[Figure 9 about here.]

4 Conclusions

The present work introduced an unsupervised machine learning framework for the spatial stratification of calcification risk on prosthetic aortic valve leaflets. Six valve configurations, arising from two scallop geometries and three constitutive material models, were simulated during systole in a patient-specific curved aorta through fully coupled fluid-structure interaction. An incremental Finite-Time Lyapunov Exponent formulation was proposed to quantify the spatial coherence of leaflet material points throughout systole and complemented by wall shear stress derived temporal features extracted from the ventricular leaflet surface.

The present study has some limitations. The FSI simulations cover a single systolic phase and do not capture the diastolic phase; however, since the temporal features fed into the clustering algorithm span the full systolic interval including deceleration, the associated flow reversal is implicitly accounted for. Furthermore, the FSI simulations do not take into

765 account cumulative fatigue over millions of cardiac cycles. Nevertheless, the strong spatial
 766 correlation between single-cycle haemodynamic indicators and explant calcification maps
 767 reported in⁴⁸, where the calibrated relationship (Eq. 14) was itself derived from a single-
 768 cycle FSI study, supports the premise that the risk patterns identified are representative of
 769 the long-term mechanical environment. Blood is modelled as a Newtonian fluid, neglecting
 770 shear-thinning rheology and platelet activation. Only one patient-specific aortic anatomy is
 771 considered; the sensitivity of the risk ranking to inter-patient anatomical variability therefore
 772 remains unquantified. However, the good agreement between the FTLE- and WSS-based
 773 clustering derived from the present curved aorta and the calcification intensity relationship
 774 calibrated on a straight aorta geometry in⁴⁸ does suggest that the proposed framework is not
 775 confined to a single aortic configuration. The k -means clustering employs a fixed number of
 776 four classes selected by silhouette analysis (Fig. S1); other algorithms or class numbers could
 777 nonetheless refine the stratification. Finally, the validation against experimentally calibrated
 778 calcification data is restricted to bovine pericardial tissue, no analogous benchmark being
 779 currently available for the elastomeric or porcine configurations.

780 The main conclusions of the present study are as follows. The FTLE and WSS descrip-
 781 tors capture complementary facets of the calcification driving mechanisms: the FTLE-based
 782 clustering penalises configurations that concentrate strain into localised high-gradient zones
 783 (porcine tissue in both geometries), whereas the WSS-based clustering penalises those sus-
 784 taining elevated mean shear through narrow orifices (D1^V-ELA, D1^V-BOV) or intense tem-
 785 poral shear variability through persistent flutter (D2^U-ELA). Notably, the porcine configu-
 786 rations rank favourably in the WSS analysis because their wide orifice diffuses the systolic
 787 jet and attenuates peak wall shear. Their combination with approximately equal weight
 788 ($w \approx 0.50$) produces a strong Spearman rank correlation $\rho_S \geq 0.86$ and a weighted kappa
 789 $\kappa_w \geq 0.72$, corresponding to substantial to near-perfect ordinal agreement for both bovine
 790 pericardial configurations, a fidelity that neither descriptor achieves individually. In this
 791 light, the D2^U geometry paired with bovine pericardium emerges as the sole configuration
 792 ranking first in both analyses, owing to suppressed leaflet flutter and limited strain locali-

sation. By contrast, the isotropic silicone-based elastomeric material distributes strain uniformly yet sustains pronounced WSS fluctuations through persistent low-frequency, small-amplitude flutter, resulting in the highest WSS-based risk scores. These opposing trends underscore the necessity of evaluating both structural and haemodynamic risk dimensions simultaneously when designing polymeric valve prostheses. Beyond material and geometry effects, the patient-specific aortic curvature induces a systematic elevation of the risk score for the leaflet seated in the sinus facing the inner (concave) aortic wall, independently of leaflet material and geometry.

The proposed framework, requiring no fitting to experimental calcification data, is directly transferable to novel valve geometries and materials. Its extension to multiple patient anatomies and to structural models accounting for cyclic fatigue and progressive tissue damage would represent a natural progression towards a comprehensive computational tool for prosthetic valve design and optimisation.

Authors' contribution

P. Corso: Conceptualisation, Methodology, Software, Formal analysis, Investigation, Data curation, Writing - original draft, Writing - review and editing, Validation, Visualisation, Resources (supercomputing allocations), Project administration.

G. Tagliavini: Investigation, Validation, Writing - review and editing.

M. G. C. Nestola: Software, Writing - review and editing.

F. B. Coulter: Resources (CAD construction of the valve leaflet and patient-specific aorta geometries; stress-strain experimental data for the elastomeric material), Writing - review and editing.

Acknowledgements

This work was supported by computational resources provided by the Swiss National Supercomputing Centre (CSCS) on the *Piz Daint* and *Daint.Alps* supercomputers under project IDs s1153, s1210 and s1284.

Declaration of competing interest

The authors declare that they have no known competing financial interests or personal relationships that could have appeared to influence the work reported in this paper.

Funding declaration

The authors received no specific funding for this work.

Ethics declaration

The aorta geometry used in this study was reconstructed from computed tomography data of a randomised patient provided by the University Hospital Zurich (USZ). The data were fully anonymised by USZ prior to being shared with the authors. Under Article 2(2)(c) of the Swiss Human Research Act (HRA), the Act does not apply to research conducted on anonymised health-related data; formal ethics committee approval was therefore not required. Individual patient consent was likewise not required, as no identifiable data were used at any stage of this work.

Data and materials availability

All data and materials needed to evaluate the findings and conclusions of this article are present in the main text or Supporting Information. The underlying FSI-derived FTLE

and WSS fields, leaflet displacement data and k -means cluster maps are available from the corresponding author upon reasonable request.

References

1. A. Arzani, S.C. Shadden, Wall shear stress fixed points in cardiovascular fluid mechanics, *J. Biomech.* 73 (2017) 145–152.
2. F. Auricchio, M. Conti, A. Ferrara, S. Morganti, A. Reali, Patient-specific simulation of a stentless aortic valve implant: the impact of fibres on leaflet performance, *Comput. Methods Biomech. Biomed. Eng.* 17 (3) (2014) 277–285.
3. S. Balay, S. Abhyankar, M.F. Adams, et al., PETSc web page, 2023, <https://petsc.org/>.
4. B. Becsek, L. Pietrasanta, D. Obrist, Turbulent systolic flow downstream of a bioprosthetic aortic valve: Velocity spectra, wall shear stresses, and turbulent dissipation rates, *Front. Physiol.* 11 (2020) 539–575.
5. P. Boloori Zadeh, S.C. Corbett, H. Nayeb-Hashemi, Effects of fluid flow shear rate and surface roughness on the calcification of polymeric heart valve leaflet, *Mater. Sci. Eng. C* 33 (5) (2013) 2770–2775.
6. A. Bonetti, M. Marchini, F. Ortolani, Ectopic mineralization in heart valves: new insights from in vivo and in vitro procalcific models and promising perspectives on non-calcifiable bioengineered valves, *J. Thorac. Dis.* 11 (5) (2019) 2126–2143.
7. M.G. Borja, P. Martinez-Legazpi, C. Nguyen, O. Flores, A.M. Kahn, J. Bermejo, J.C. Del Álamo, Deriving phenotype-representative left ventricular flow patterns by reduced-order modelling and classification, *Computers in Biology and Medicine* 179 (2024) 108760.
8. A.D. Caballero, S. Laín, A review on computational fluid dynamics modelling in human thoracic aorta, *Cardiovasc. Eng. Technol.* 4 (2) (2013) 103–130.

9. S. Chandra, N.M. Rajamannan, P. Sucosky, Computational assessment of bicuspid aortic valve wall-shear stress: implications for calcific aortic valve disease, *Biomechanics and Modeling in Mechanobiology* 11 (2012) 1085–1096
10. P. Corso, J. Walheim, H. Dillinger, et al., Toward an accurate estimation of wall shear stress from 4D flow magnetic resonance downstream of a severe stenosis, *Magn. Reson. Med.* 86 (3) (2021) 1531–1543.
11. P. Corso, D. Obrist, On the role of aortic valve architecture for physiological hemodynamics and valve replacement, Part I: Flow configuration and vortex dynamics, *Comput. Biol. Med.* 176 (2024) 108526.
12. P. Corso, D. Obrist, On the role of aortic valve architecture for physiological hemodynamics and valve replacement, Part II: Spectral analysis and anisotropy, *Comput. Biol. Med.* 176 (2024) 108552.
13. M.C.B. Costa, S.D.F. Gonçalves, M.L.F.D. Silva, J.V.C. Fleury, R. Huebner, A.H.D.F. Avelar, The influence of leaflet flutter of the aortic valve bioprostheses on leaflet calcification and endothelial activation, *Comput. Biol. Med.* 187 (2025) 109765.
14. F.B. Coulter, M. Schaffner, J.A. Faber, et al., Bioinspired heart valve prosthesis made by silicone additive manufacturing, *Matter* 1 (2019) 266–279.
15. A. Falahatpisheh, A. Jocelyn, A. Kheradvar, et al., Calcification of polymeric heart valve leaflets, *J. Biomech.* (2017).
16. S. Glaßer, K. Lawonn, T. Hoffmann, M. Skalej, B. Preim, Combined visualization of wall thickness and wall shear stress for the evaluation of aneurysms, *IEEE Transactions on Visualization and Computer Graphics* 20 (12) (2014) 2506–2515
17. G. Greco, P. Gaziano, S. Anglese, S. Morganti, C. de Vincentiis, F. Auricchio, M. Marino, M. Conti, From clinic to computation: multiscale bioengineering strategies for durable biological aortic valve replacements, *Adv. Funct. Mater.* (2026) e29555.

- 883 18. C. Hahn, M.A. Schwartz, Mechanotransduction in vascular physiology and atherogenesis,
884 *Nat. Rev. Mol. Cell Biol.* 10 (1) (2009) 53–62.
- 885 19. R. Henniger, D. Obrist, L. Kleiser, High-order accurate solution of the incompressible
886 Navier–Stokes equations on massively parallel computers, *J. Comput. Phys.* 229 (10)
887 (2010) 3543–3572.
- 888 20. D.F. Hernandez-Suarez, Y. Kim, P. Villablanca, T. Gupta, J. Wiley, B.G. Nieves-
889 Rodriguez, J. Rodriguez-Maldonado, R. Feliu Maldonado, I. da Luz Sant’Ana, C. San-
890 ina, P. Cox-Alomar, H. Ramakrishna, A. Lopez-Candales, W.W. O’Neill, D.S. Pinto, A.
891 Latib, A. Roche-Lima, Machine learning prediction models for in-hospital mortality af-
892 ter transcatheter aortic valve replacement, *JACC: Cardiovascular Interventions* 12 (14)
893 (2019) 1328–1338
- 894 21. G. Holste , E.K. Oikonomou, B.J. Mortazavi, A. Coppi, K.F. Faridi, E.J. Miller, J.K.
895 Forrest, R.L. McNamara, L. Ohno-Machado, N. Yuan, A. Gupta, D. Ouyang, H.M.
896 Krumholz, Z. Wang, R. Khera, Severe aortic stenosis detection by deep learning applied
897 to echocardiography, *European Heart Journal* 44 (43) (2023) 4592–4604
- 898 22. G.A. Holzapfel, Th.C. Gasser, R.W. Ogden, A new constitutive framework for arterial
899 wall mechanics and a comparative study of material models, *J. Elasticity* 61 (1) (2000)
900 1–48.
- 901 23. E.L. Johnson, M.C.H. Wu, F. Xu, N.M. Wiese, M.R. Rajanna, A.J. Herrema, B. Gana-
902 pathysubramanian, T.J.R. Hughes, M.S. Sacks, M.-C. Hsu, Thinner biological tissues
903 induce leaflet flutter in aortic heart valve replacements, *Proc. Natl. Acad. Sci. U.S.A.*
904 117 (32) (2020) 19007–19016.
- 905 24. E.L. Johnson, M.R. Rajanna, C.-H. Yang, M.-C. Hsu, Effects of membrane and flexural
906 stiffnesses on aortic valve dynamics: identifying the mechanics of leaflet flutter in thinner
907 biological tissues, *Forces Mech.* 6 (2022) 100053.

25. A.E. Kostyunin, A.E. Yuzhalin, M.A. Rezvova, E.A. Ovcharenko, T.V. Glushkova, A.G. Kutikhin, Degeneration of bioprosthetic heart valves: update 2020, *J. Am. Heart Assoc.* 9 (2020) e018506.
26. R. Krause, P. Zulian, A parallel approach to the variational transfer of discrete fields between arbitrarily distributed unstructured finite element meshes, *SIAM J. Sci. Comput.* 38 (3) (2016).
27. J. Kwiecinski, M. Dabrowski, L. Nombela-Franco, K. Grodecki, K. Pieszko, Z. Chmielak, A. Pylko, B. Hennessey, L. Kalinczuk, G. Tirado-Conte, B. Rymuza, J. Kochman, M.P. Opolski, Z. Huczek, M.R. Dweck, D. Dey, P. Jimenez-Quevedo, P. Slomka, A. Witkowski, Machine learning for prediction of all-cause mortality after transcatheter aortic valve implantation, *European Heart Journal – Quality of Care and Clinical Outcomes* 9 (8) (2023) 768–777.
28. J.R. Landis, G.G. Koch, The measurement of observer agreement for categorical data, *Biometrics* 33 (1) (1977) 159–174.
29. S.E. Langdon, R. Chernecky, C.A. Pereira, D. Abdulla, J.M. Lee, Biaxial mechanical/structural effects of equibiaxial strain during crosslinking of bovine pericardial xenograft materials, *Biomaterials* 20 (2) (1999) 137–153.
30. C. Laville, C. Pradille, Y. Tillier, Mechanical characterization and identification of material parameters of porcine aortic valve leaflets, *J. Mech. Behav. Biomed. Mater.* 112 (2020) 104036.
31. J.B. MacQueen, Some methods for classification and analysis of multivariate observations, in: *Proc. 5th Berkeley Symp. Math. Statist. Prob.*, 1967, pp. 281–297.
32. V. Mazzi, D. Gallo, K. Calò, et al., A Eulerian method to analyze wall shear stress fixed points and manifolds in cardiovascular flows, *Biomech. Model. Mechanobiol.* 19 (5) (2020) 1403–1423.

- 933 33. M. Meuschke, S. Oeltze-Jafra, O. Beuing, B. Preim, K. Lawonn, Classification of blood
934 flow patterns in cerebral aneurysms, *IEEE Transactions on Visualization and Computer*
935 *Graphics* 25 (7) (2019) 2404–2418
- 936 34. S. Morizawa, K. Shimoyama, S. Obayashi, K. Funamoto, T. Hayase, Implementation
937 of visual data mining for unsteady blood flow field in an aortic aneurysm, *Journal of*
938 *Visualization* 14 (4) (2011) 393–398
- 939 35. K. Murdock, C. Martin, W. Sun, Characterization of mechanical properties of peri-
940 cardium tissue using planar biaxial tension and flexural deformation, *J. Mech. Behav.*
941 *Biomed. Mater.* 77 (2018) 148–156.
- 942 36. M.G.C. Nestola, B. Becsek, H. Zolfaghari, et al., An immersed boundary method for
943 fluid-structure interaction based on variational transfer, *J. Comput. Phys.* 398 (2019).
- 944 37. M.G.C. Nestola, P. Zulian, L. Gaedke-Merzhäuser, R. Krause, Fully coupled dynamic
945 simulations of bioprosthetic aortic valves based on an embedded strategy for fluid–
946 structure interaction with contact, *Europace* 23 (2021).
- 947 38. V. Nguyen, M. Michel, H. Eltchaninoff, et al., Implementation of transcatheter aortic
948 valve replacement in France, *J. Am. Coll. Cardiol.* 71 (15) (2018).
- 949 39. V.T. Nkomo, J.M. Gardin, T.N. Skelton, et al., Burden of valvular heart diseases: a
950 population-based study, *Lancet* 368 (9540) (2006) 1005–1011.
- 951 40. A.B. Olcay, A. Amindari, K. Kirkkopru, H.C. Yalcin, Characterization of disturbed
952 hemodynamics due to stenosed aortic jets with a Lagrangian coherent structures tech-
953 nique, *J. Appl. Fluid Mech.* 11 (2) (2018) 375–384.
- 954 41. F. Oveissi, S. Naficy, A. Lee, D.S. Winlaw, F. Dehghani, Materials and manufacturing
955 perspectives in engineering heart valves: a review, *Mater. Today Bio* 5 (2020) 100038.
- 956 42. F. Pedregosa, G. Varoquaux, A. Gramfort, et al., Scikit-learn: Machine Learning in
957 Python, *J. Mach. Learn. Res.* 12 (2011) 2825–2830.

- 958 43. C.J. Permann, D.R. Gaston, D. Andrs, et al., MOOSE: Enabling massively parallel
959 multiphysics simulation, *SoftwareX* 11 (2020).
- 960 44. M.A. Rezvova, K.Y. Klyshnikov, A.A. Gritskevich, Polymeric heart valves will displace
961 mechanical and tissue heart valves: a new era for the medical devices, *Int. J. Mol. Sci.*
962 24 (2023) 3963.
- 963 45. E. Salaün, M.-A. Clavel, J.-L. Rodés-Cabau, P. Pibarot, Bioprosthetic aortic valve dura-
964 bility in the era of transcatheter aortic valve implantation, *Heart* 104 (2018) 1323–1332.
- 965 46. F.J. Schoen, R.J. Levy, Calcification of tissue heart valve substitutes: progress toward
966 understanding and prevention, *Ann. Thorac. Surg.* 79 (2005) 1072–1080.
- 967 47. S.C. Shadden, M. Astorino, J.-F. Gerbeau, Computational analysis of an aortic valve jet
968 with Lagrangian coherent structures, *Chaos* 20 (2010) 1–11.
- 969 48. E. Tsolaki, P. Corso, R. Zboray, J. Avaro, et al., Multiscale multimodal characteriza-
970 tion and simulation of structural alterations in failed bioprosthetic heart valves, *Acta*
971 *Biomater.* 169 (10) (2023) 138–154.
- 972 49. A. Whelan, E. Williams, E. Fitzpatrick, et al., Collagen fibre-mediated mechanical dam-
973 age increases calcification of bovine pericardium for use in bioprosthetic heart valves,
974 *Acta Biomater.* 128 (2021) 384–393.
- 975 50. P. Yevtushenko, L. Goubergrits, B. Franke, T. Kuehne, M. Schafstedde, Modelling blood
976 flow in patients with heart valve disease using deep learning: a computationally efficient
977 method to expand diagnostic capabilities in clinical routine, *Frontiers in Cardiovascular*
978 *Medicine* 10 (2023) 1136935

List of Figures

- 1 Parametrisation of the two leaflet geometries. (A) Three-dimensional view of the valve with three leaflets attached to the crown in the patient-specific aorta. The leaflet surface is generated by sweeping and blending the belly curve (hyperbolic sine, red) and the scallop curve (power law, blue). (B) Side views of D1^V and D2. (C) Normalised belly height as a function of the normalised coordinate for D1^V ($a_{\sinh} = 0.91$, $b_{\sinh} = 1.05$) and D2^U ($a_{\sinh} = 0.89$, $b_{\sinh} = 1.04$). (D) Normalised scallop height for D1^V ($n^{\text{power}} = 2.08$) and D2^U ($n^{\text{power}} = 4.68$). 42
- 2 Geometrical description and numerical setup for the FSI simulations. (A) Two valve geometries (D1, D2) with the key anatomical features indicated (leaflet, crown, tip, belly, base, commissures) and the patient-specific curved aorta including the LVOT, sinus and curved ascending aorta. (B) Computational domain: Cartesian fluid grid ($55 \times 65 \times 110 \text{ mm}^3$, ~ 47 million points), tetrahedral solid mesh ($\sim 280,000$ elements) and cylindrical fringe regions for imposing a prescribed pressure difference. Inset: flow rate Q [L/min] and orifice Reynolds number Re_{orifice} versus non-dimensional time t^* . Blood is modelled as a Newtonian fluid and the aorta as an incompressible Neo-Hookean material. Reference velocity $U_0 = 0.772 \text{ m/s}$; reference length $\mathcal{L}_0 = \mathcal{D} = 0.022 \text{ m}$. 43
- 3 Material characterisation of the three leaflet constitutive models. (A) Engineering stress versus stretch for the elastomeric material (ELA, Mooney-Rivlin), bovine pericardium (BOV, HGO, circumferential and axial) and porcine tissue (PORC, exp-HGO, circumferential and axial). Experimental data with error bars are shown for the elastomer. (B) Comparison of the porcine exp-HGO model employed in the FSI simulations against experimental data from porcine pericardium (Murdock *et al.*³⁵) and native porcine leaflets (Laville *et al.*³⁰). (C) Visualisation of the two fibre families oriented at $\pm\beta$ with respect to the circumferential direction $\mathbf{e}_{\text{circum}}$ on the bovine pericardial leaflet surface. 44
- 4 Time series of the spatially averaged displacement magnitude of the leaflet mesh nodes (averaged over all three cusps) measured from the initial leaflet position at $t = 0 \text{ s}$ for the three material models (A) D1^V geometry. (B) D2^U geometry. The displacement magnitude encompasses both leaflet deformation and the rigid-body translation of the valve ring induced by aortic wall motion. 45
- 5 Instantaneous WSS magnitude $\|\mathbf{WSS}\|$ [Pa] on the ventricular side of the leaflets and flow streamlines coloured by velocity magnitude $\|\mathbf{v}\|$ [m/s] at five time instants during systole ($t = 0.05, 0.10, 0.15, 0.20$ and 0.25 s) for (A) elastomeric, (B) bovine pericardial and (C) porcine tissue leaflets. Within each panel, D1^V is shown at top and D2^U at bottom. The maximum velocity U_{max} [m/s] for the streamline colour scale at each time instant is indicated above each column. 46

1019	6	FTLE-based calcification risk clusters on the aortic surface of the three leaflets	
1020		for all six valve configurations, obtained from k -means clustering with $K = 4$.	
1021		Clusters: low (green), medium-low (purple), medium-high (orange), high	
1022		(red). The per-leaflet risk score RS is reported below each leaflet. Con-	
1023		figurations are ordered by increasing overall risk score from top to bottom. .	47
1024	7	WSS-based calcification risk clusters on the aortic surface of the three leaflets	
1025		for all six valve configurations, obtained from k -means clustering with $K = 4$.	
1026		Cluster labels and colour coding as in Fig. 6. The ordering of configurations	
1027		differs from the FTLE-based ranking.	48
1028	8	Validation of the k -means clustering against experimentally calibrated calcifi-	
1029		cation data for the D1 ^V -BOV configuration. Rows: three leaflets (L1, L2, L3).	
1030		Columns from left to right: risk levels from quartiles of the experimentally	
1031		calibrated calcification intensity ⁴⁸ ; FTLE-based clusters; WSS-based clusters;	
1032		arithmetic mean of FTLE- and WSS-based cluster indices. Spearman rank	
1033		correlation coefficients ρ_S are indicated at the bottom of each column.	49
1034	9	Overall calcification risk scores ranked in ascending order for (A) the FTLE-	
1035		-based analysis, constructed from the temporal-minimum FTLE and its spa-	
1036		tial gradients across the leaflet mesh, and (B) the WSS-based analysis, con-	
1037		structed from the time-averaged WSS magnitude and the temporal standard	
1038		deviation of $\ \mathbf{WSS}\ $ on the ventricular side of the leaflets.	50

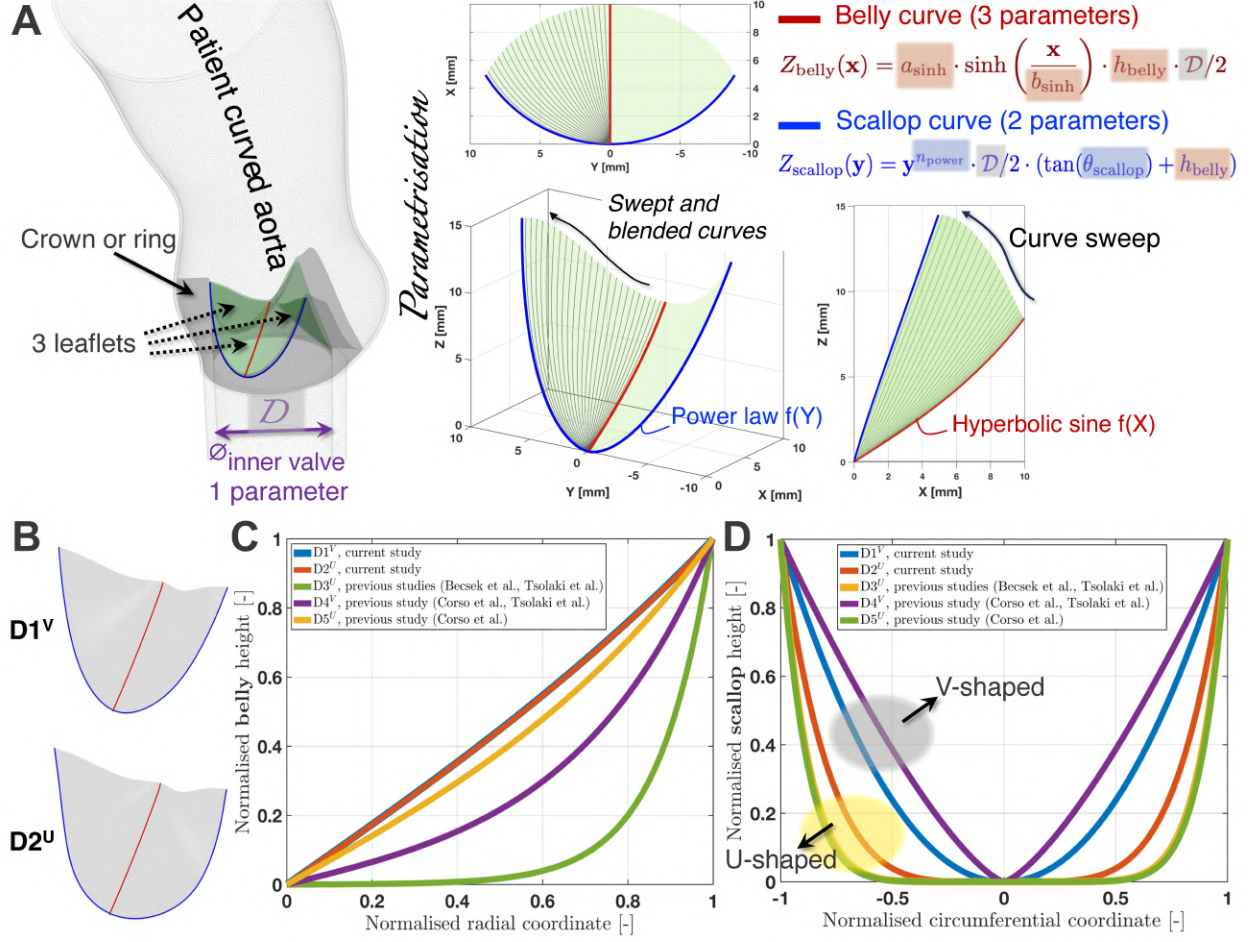


Figure 1: Parametrisation of the two leaflet geometries. (A) Three-dimensional view of the valve with three leaflets attached to the crown in the patient-specific aorta. The leaflet surface is generated by sweeping and blending the belly curve (hyperbolic sine, red) and the scallop curve (power law, blue). (B) Side views of $D1^V$ and $D2^U$. (C) Normalised belly height as a function of the normalised coordinate for $D1^V$ ($a_{\text{sinh}} = 0.91$, $b_{\text{sinh}} = 1.05$) and $D2^U$ ($a_{\text{sinh}} = 0.89$, $b_{\text{sinh}} = 1.04$). (D) Normalised scallop height for $D1^V$ ($n^{\text{power}} = 2.08$) and $D2^U$ ($n^{\text{power}} = 4.68$).

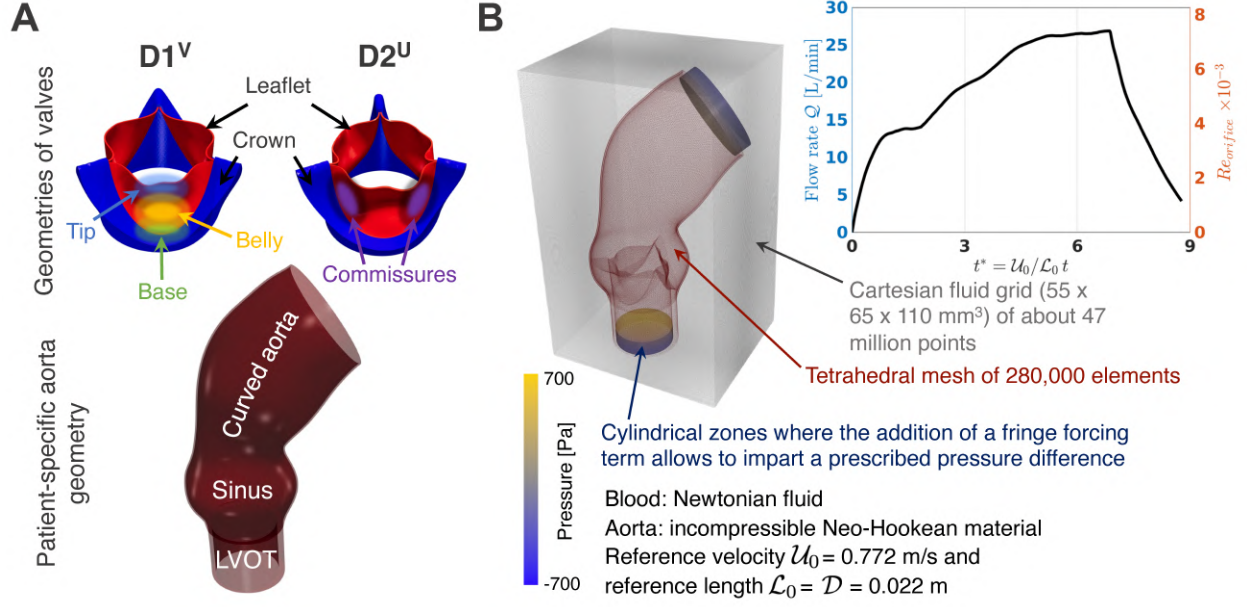


Figure 2: Geometrical description and numerical setup for the FSI simulations. **(A)** Two valve geometries (D1, D2) with the key anatomical features indicated (leaflet, crown, tip, belly, base, commissures) and the patient-specific curved aorta including the LVOT, sinus and curved ascending aorta. **(B)** Computational domain: Cartesian fluid grid ($55 \times 65 \times 110$ mm³, ~ 47 million points), tetrahedral solid mesh ($\sim 280,000$ elements) and cylindrical fringe regions for imposing a prescribed pressure difference. Inset: flow rate Q [L/min] and orifice Reynolds number Re_{orifice} versus non-dimensional time t^* . Blood is modelled as a Newtonian fluid and the aorta as an incompressible Neo-Hookean material. Reference velocity $\mathcal{U}_0 = 0.772$ m/s; reference length $\mathcal{L}_0 = \mathcal{D} = 0.022$ m.

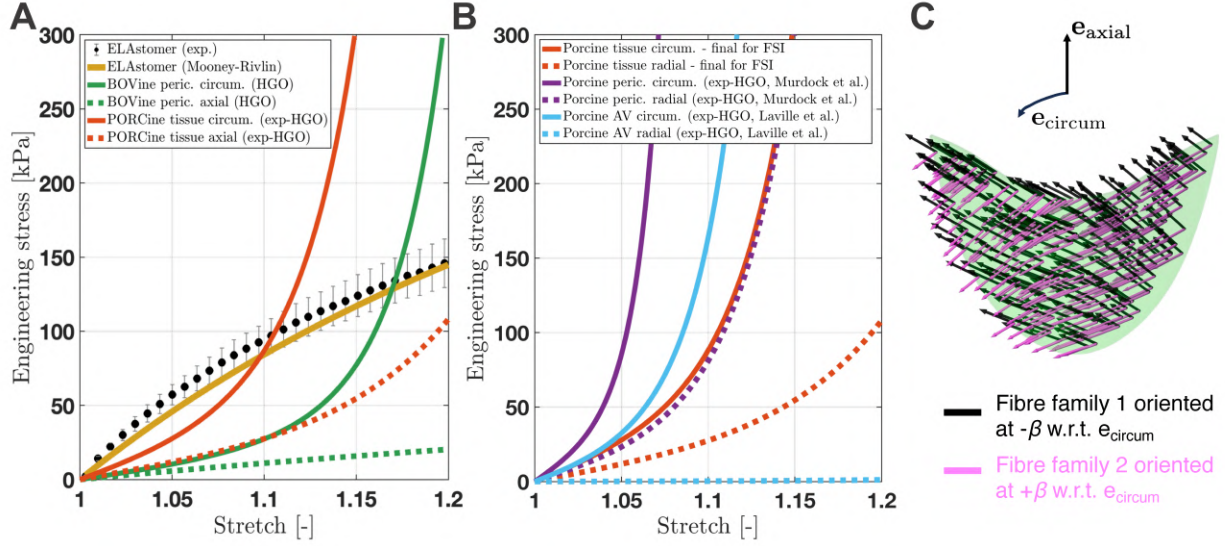


Figure 3: Material characterisation of the three leaflet constitutive models. (A) Engineering stress versus stretch for the elastomeric material (ELA, Mooney-Rivlin), bovine pericardium (BOV, HGO, circumferential and axial) and porcine tissue (PORC, exp-HGO, circumferential and axial). Experimental data with error bars are shown for the elastomer. (B) Comparison of the porcine exp-HGO model employed in the FSI simulations against experimental data from porcine pericardium (Murdock *et al.*³⁵) and native porcine leaflets (Laville *et al.*³⁰). (C) Visualisation of the two fibre families oriented at $\pm\beta$ with respect to the circumferential direction e_{circum} on the bovine pericardial leaflet surface.

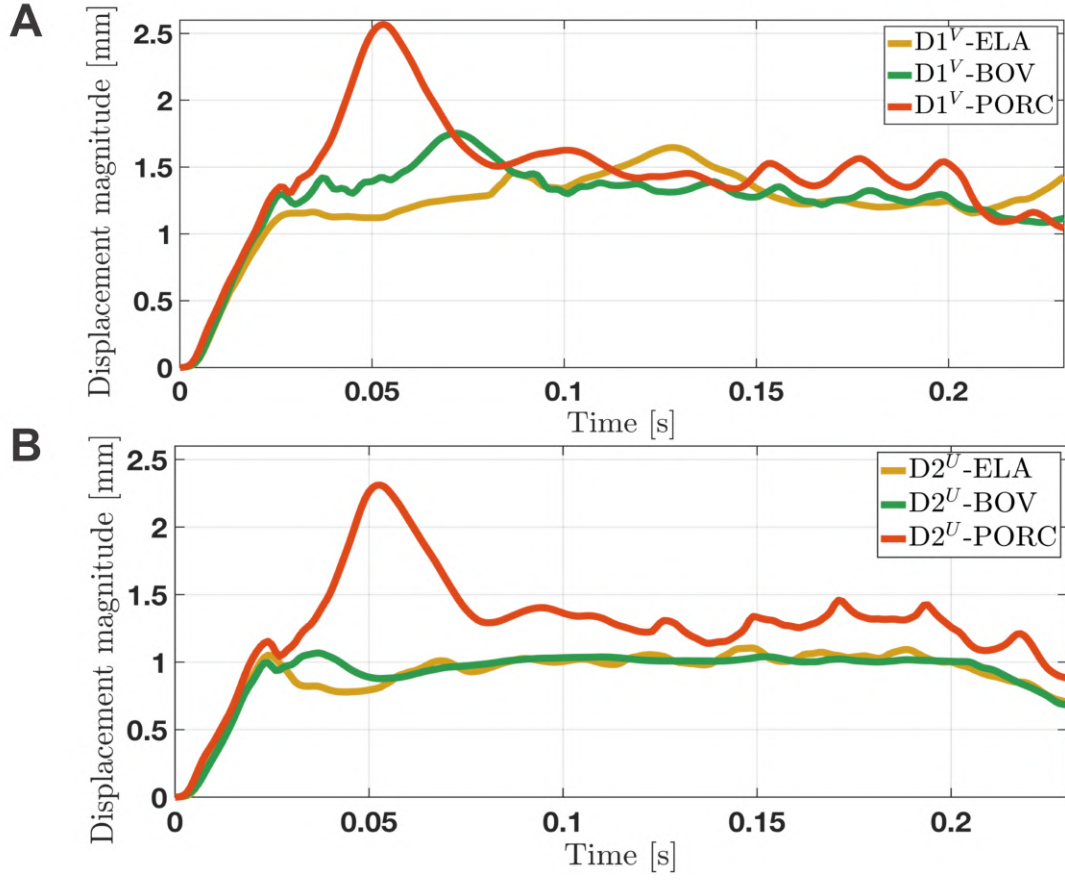


Figure 4: Time series of the spatially averaged displacement magnitude of the leaflet mesh nodes (averaged over all three cusps) measured from the initial leaflet position at $t = 0$ s for the three material models (A) D1^V geometry. (B) D2^U geometry. The displacement magnitude encompasses both leaflet deformation and the rigid-body translation of the valve ring induced by aortic wall motion.

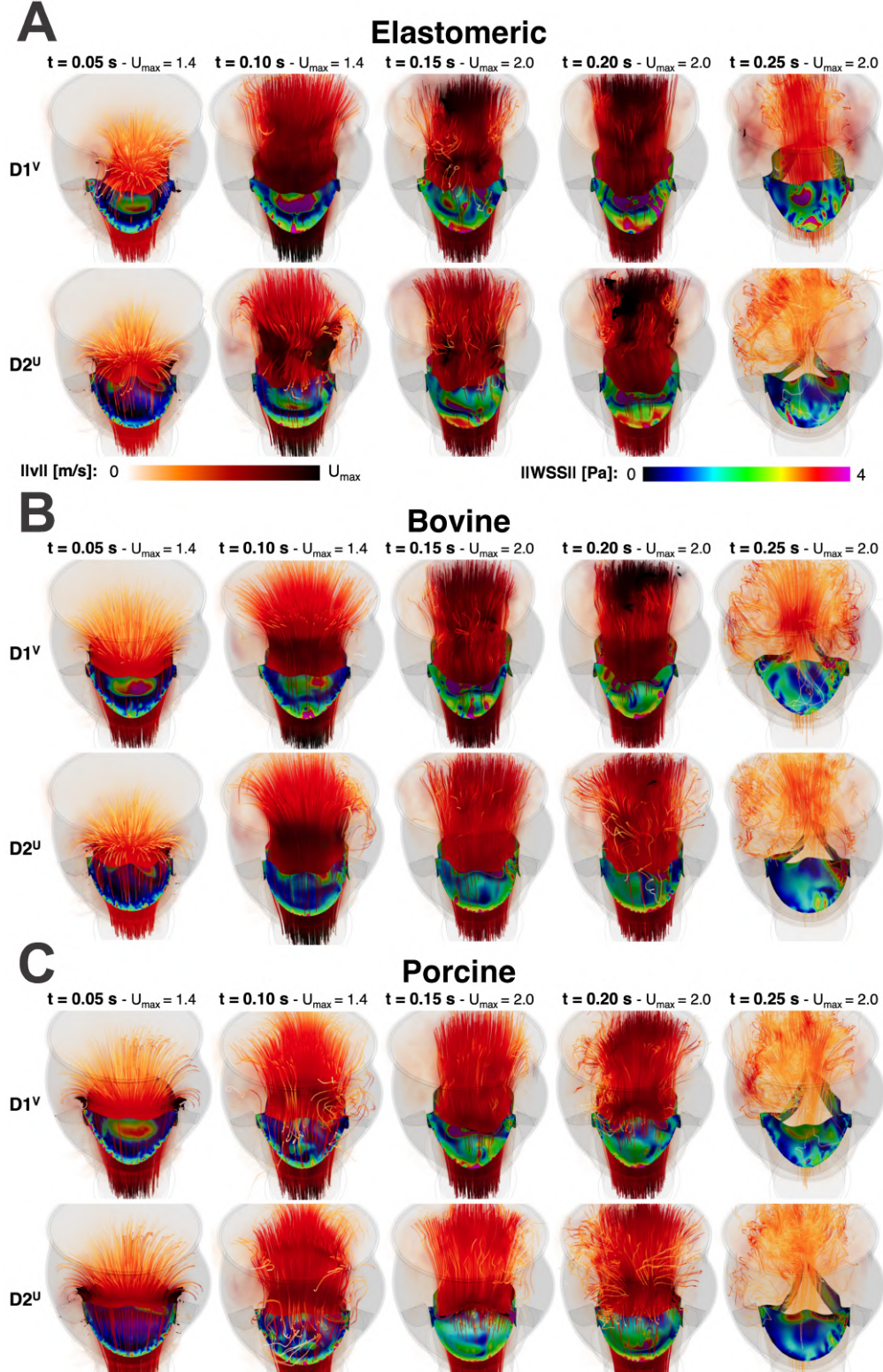


Figure 5: Instantaneous WSS magnitude $\|\mathbf{WSS}\|$ [Pa] on the ventricular side of the leaflets and flow streamlines coloured by velocity magnitude $\|\mathbf{v}\|$ [m/s] at five time instants during systole ($t = 0.05, 0.10, 0.15, 0.20$ and 0.25 s) for (A) elastomeric, (B) bovine pericardial and (C) porcine tissue leaflets. Within each panel, $D1^V$ is shown at top and $D2^U$ at bottom. The maximum velocity U_{\max} [m/s] for the streamline colour scale at each time instant is indicated above each column.

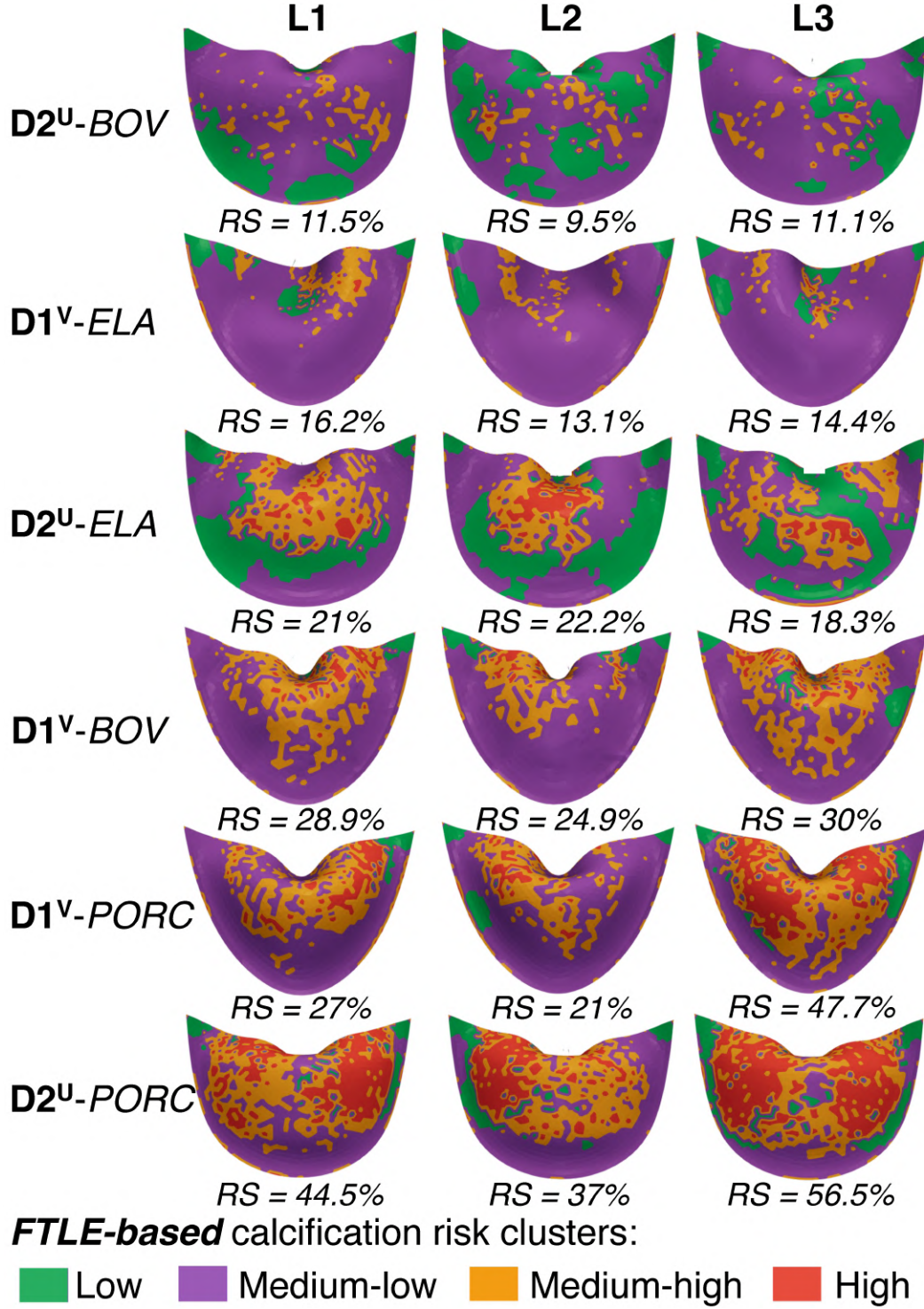


Figure 6: FTLE-based calcification risk clusters on the aortic surface of the three leaflets for all six valve configurations, obtained from k -means clustering with $K = 4$. Clusters: low (green), medium-low (purple), medium-high (orange), high (red). The per-leaflet risk score RS is reported below each leaflet. Configurations are ordered by increasing overall risk score from top to bottom.

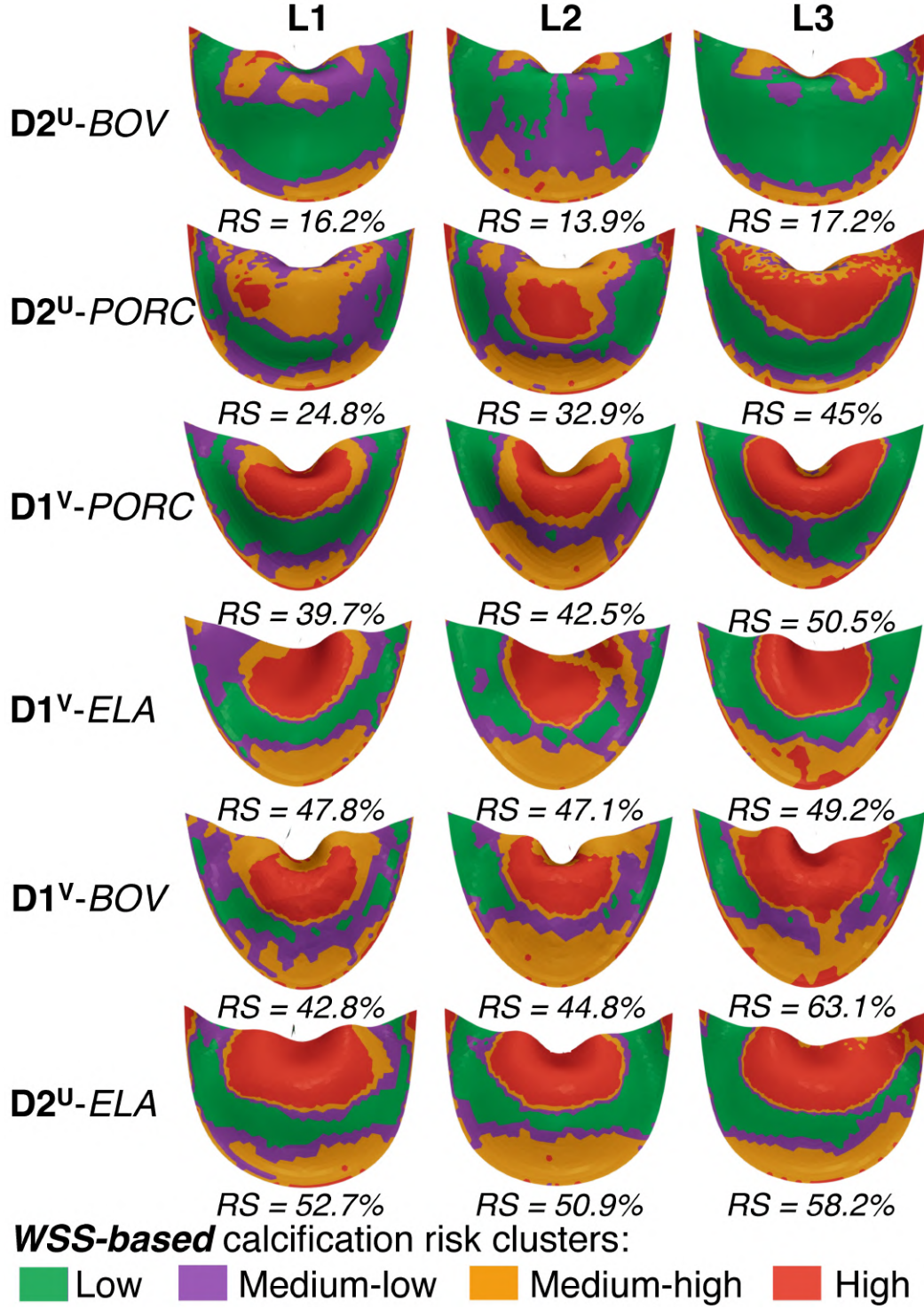


Figure 7: WSS-based calcification risk clusters on the aortic surface of the three leaflets for all six valve configurations, obtained from k -means clustering with $K = 4$. Cluster labels and colour coding as in Fig. 6. The ordering of configurations differs from the FTLE-based ranking.

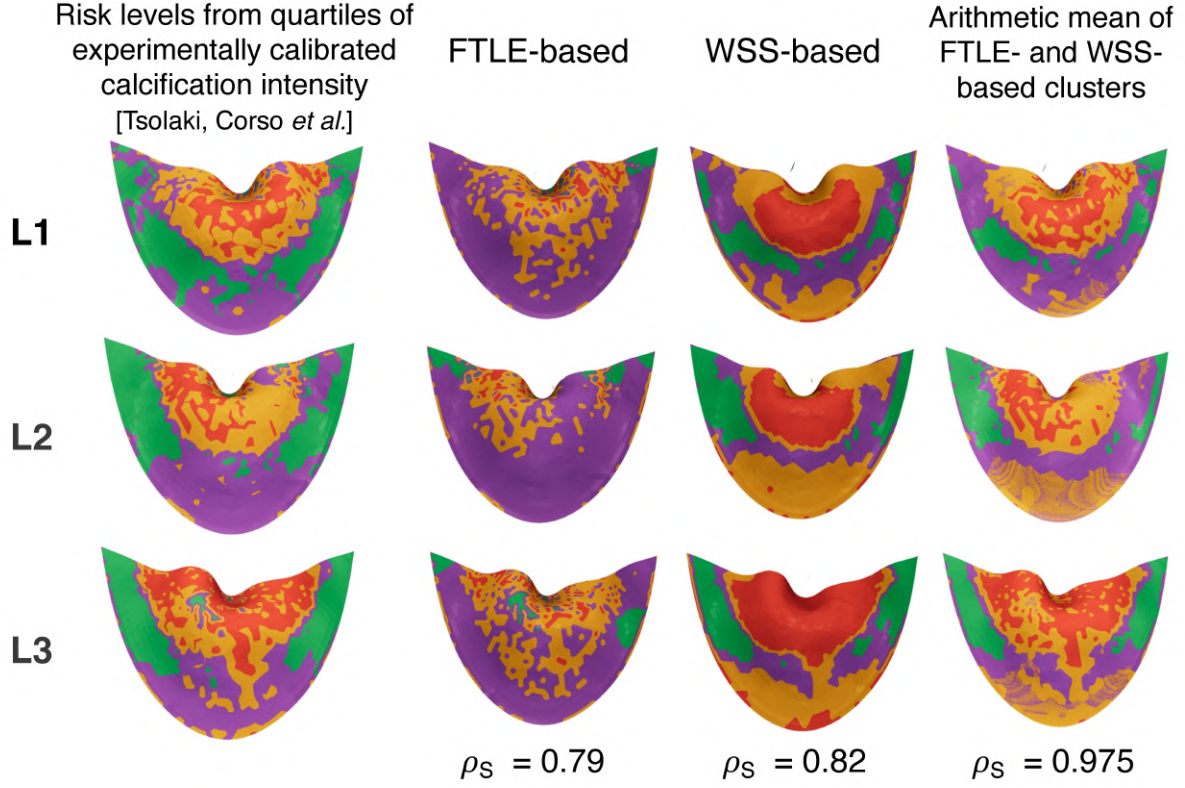


Figure 8: Validation of the k -means clustering against experimentally calibrated calcification data for the D1^V-BOV configuration. Rows: three leaflets (L1, L2, L3). Columns from left to right: risk levels from quartiles of the experimentally calibrated calcification intensity⁴⁸; FTLE-based clusters; WSS-based clusters; arithmetic mean of FTLE- and WSS-based cluster indices. Spearman rank correlation coefficients ρ_S are indicated at the bottom of each column.

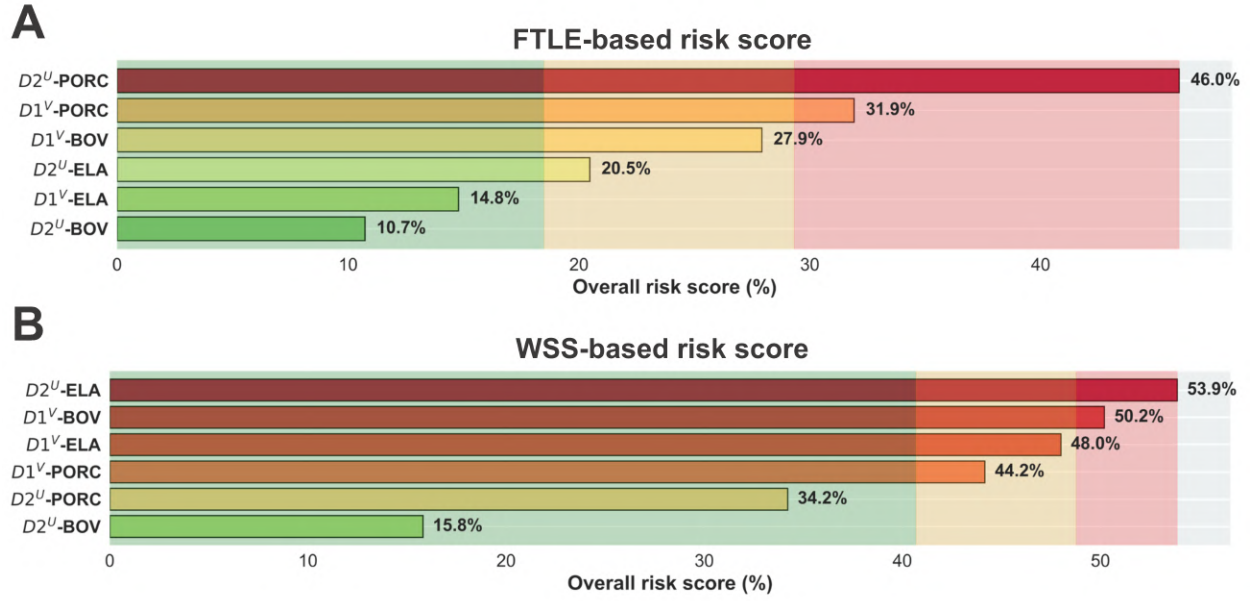


Figure 9: Overall calcification risk scores ranked in ascending order for (A) the FTLE-based analysis, constructed from the temporal-minimum FTLE and its spatial gradients across the leaflet mesh, and (B) the WSS-based analysis, constructed from the time-averaged WSS magnitude and the temporal standard deviation of $\|\mathbf{WSS}\|$ on the ventricular side of the leaflets.

List of Tables

1039			
1040	1	Summary of the leaflet geometry parameters for the five valve leaflet designs	
1041		considered in this work. The parameters a_{sinh} and b_{sinh} govern the normalised	
1042		belly curve (Eq. (1)), h_{belly} is the belly height factor, n_{power} is the power-law	
1043		exponent of the scallop curve (Eq. (2)), θ_{scallop} is the scallop inclination angle,	
1044		\mathcal{D} is the valve inner diameter, L_{belly} is the belly length and \mathcal{T} is the leaflet	
1045		thickness. Designs D1 ^V and D2 ^U are introduced in the present study; D3 ^U ,	
1046		D4 ^V and D5 ^U correspond to the leaflet geometries previously denoted ULth0,	
1047		VLth30 and Ulth0, respectively ^{11,48}	52
1048	2	Material parameters of the three constitutive models adopted for the valve	
1049		leaflet response.	53
1050	3	Summary of flutter and flapping characteristics for the six valve configura-	
1051		tions during systole. N/A: no discernible oscillation. [†] Peak amplitude of	
1052		intermittent single-leaflet oscillations; no sustained flutter regime is present. .	54

Table 1: Summary of the leaflet geometry parameters for the five valve leaflet designs considered in this work. The parameters a_{sinh} and b_{sinh} govern the normalised belly curve (Eq. (1)), h_{belly} is the belly height factor, n_{power} is the power-law exponent of the scallop curve (Eq. (2)), θ_{scallop} is the scallop inclination angle, \mathcal{D} is the valve inner diameter, L_{belly} is the belly length and \mathcal{T} is the leaflet thickness. Designs D1^V and D2^U are introduced in the present study; D3^U, D4^V and D5^U correspond to the leaflet geometries previously denoted ULth0, VLth30 and Ulth0, respectively^{11,48}.

Design	a_{sinh} [-]	b_{sinh} [-]	h_{belly} [-]	n_{power} [-]	θ_{scallop} [°]	\mathcal{D} [mm]	L_{belly} [mm]	\mathcal{T} [μm]
D1 ^V	0.91	1.05	0.89	2.08	19.8	22	14.5	300
D2 ^U	0.89	1.04	0.89	4.68	19.5	22	14.5	300
D3 ^U	6×10^{-4}	0.123	1.17	7.99	7.08	18	14.6	500
D4 ^V	0.104	0.338	1.24	1.37	15.9	18	14.5	500
D5 ^U	0.453	0.652	1.18	8.39	7.3	18	13	500

Table 2: Material parameters of the three constitutive models adopted for the valve leaflet response.

Model	Parameter	Value	Unit
ELA (Mooney-Rivlin, Eq. 3)	C_{10}^{MR}	23.4	kPa
	C_{01}^{MR}	140.8	kPa
BOV (HGO, Eq. 4)	C_{10}^{HGO}	20.1	kPa
	k_1^{HGO}	54.62	kPa
	k_2^{HGO}	30.86	—
	β	30	°
PORC (exp-HGO, Eq. 5)	C_{10}^{eHGO}	4.0	kPa
	C_{01}^{eHGO}	9.6	—
	C_2^{eHGO}	128.0	kPa
	C_3^{eHGO}	29.4	—
	κ	0	—
	θ	26	°

Table 3: Summary of flutter and flapping characteristics for the six valve configurations during systole. N/A: no discernible oscillation. [†]Peak amplitude of intermittent single-leaflet oscillations; no sustained flutter regime is present.

Configuration	Regime	Time interval [s]	Frequency [Hz]	Amplitude [mm]
D1 ^V -PORC	Low-freq. flapping	0.134–0.20	≈ 45	≈ 2.0
D1 ^V -BOV	High-freq. flutter	0.037–0.055, 0.092–0.11	≈ 330	≈ 0.4
	Low-freq. flapping	0.12–0.20	≈ 55	≈ 1.0
D1 ^V -ELA	Intermittent (single leaflet)	–	–	$\approx 1.0^{\dagger}$
D2 ^U -PORC	Low-freq. flapping	0.127–0.21	≈ 45	≈ 1.0
D2 ^U -BOV	None	–	N/A	N/A
D2 ^U -ELA	Low-freq., low-ampl. sustained flutter	0.068–0.19	45–60	0.6–0.8